NASA TECHNICAL NOTE

NASA TN D-6097

THEORETICAL ANALYSIS AND MEASUREMENT OF SINGLE-PHASE PRESSURE LOSSES AND HEAT TRANSFER FOR HELICAL FLOW IN A TUBE

by

Martin U. Gutstein
Lewis Research Center

and

George L. Converse and Jerry R. Peterson
General Electric Company

NATIONAL AERONAUTICS AND SPACE ADMINISTRATION • WASHINGTON, D. C. • NOVEMBER 1970

1. Report No.	2. Government Accession No.	3. Recipient's Catalog No.
NASA TN D-6097		

4. Title and Subtitle	5. Report Date
THEORETICAL ANALYSIS AND MEASUREMENT OF SINGLE-PHASE PRESSURE LOSSES AND HEAT TRANSFER FOR HELICAL FLOW IN A TUBE	November 1970
	6. Performing Organization Code

7. Author(s)	8. Performing Organization Report No.
Martin U. Gutstein, Lewis Research Center; George L. Converse, and Jerry R. Peterson, General Electric Co., Cincinnati, Ohio	E-5743
	10. Work Unit No. 120-27
9. Performing Organization Name and Address Lewis Research Center National Aeronautics and Space Administration Cleveland, Ohio 44135	11. Contract or Grant No.
	13. Type of Report and Period Covered Technical Note
12. Sponsoring Agency Name and Address National Aeronautics and Space Administration Washington, D.C. 20546	14. Sponsoring Agency Code

15. Supplementary Notes

16. Abstract

An analysis of flow inside a tube containing a helical-vane insert was conducted based on solid-body rotation. Equations were derived for the momentum and frictional pressure losses for fully developed flow in these inserts. Modified plain-tube expressions for friction factor and Stanton-Prandtl modulus, obtained from the analysis, were used to predict the performance of tubes with helical-vane inserts. Experimentally determined friction factors and Stanton-Prandtl moduli, obtained with four different inserts over a Reynolds number range of 30×10^3 to 300×10^3, were found to deviate from the predictions by about ±20 and ±15 percent, respectively, suggesting the analysis to be largely correct. A similar approach for other swirl-generating inserts yielded reasonable agreement of experimental data with predictions.

17. Key Words (Suggested by Author(s))	18. Distribution Statement
Helical flow Swirl flow Heat transfer Pressure loss Friction factor	Unclassified - unlimited

19. Security Classif. (of this report)	20. Security Classif. (of this page)	21. No. of Pages	22. Price*
Unclassified	Unclassified	57	$3.00

*For sale by the Clearinghouse for Federal Scientific and Technical Information
Springfield, Virginia 22151

THEORETICAL ANALYSIS AND MEASUREMENT OF SINGLE-PHASE PRESSURE LOSSES AND HEAT TRANSFER FOR HELICAL FLOW IN A TUBE

by Martin U. Gutstein, George L. Converse*, and Jerry R. Peterson*

Lewis Research Center

SUMMARY

An analysis was conducted to provide a theoretical basis for predicting the pressure losses and heat-transfer coefficients for flow in tubes containing helical-vane inserts from corresponding plain-tube data. Conservation of both linear and angular momentum was applied to a control volume, with solid-body rotation assumed. The analysis resulted in a new equation for fully developed, helical-flow momentum pressure losses, an equation for the frictional pressure losses in tubes containing helical-vane inserts, and a new, theoretically based expression for the hydraulic diameter of tubes with helical inserts. Modified plain-tube expressions for the friction factor and Stanton-Prandtl modulus for the helical-vane insert were obtained from the analysis.

Overall static-pressure losses and local heat-transfer coefficients for air flowing in a tube were determined for four different full-length helical-vane inserts. The pitch to tube diameter ratios of the inserts were 0.52, 0.75, 1.46, and 6.36. The tests were conducted over a range of Reynolds numbers of at least 30×10^3 to 300×10^3. In addition, pressure loss and heat-transfer data were obtained from a limited series of tests with a helical vane-without-centerbody insert and two wire-wrapped plugs. These inserts represented geometrical extremes of the helical-vane insert.

Friction factors, Stanton-Prandtl moduli, and Reynolds numbers were computed from the experimental data for the four helical-vane inserts. These were compared with the modified plain-tube expressions obtained from the analysis. The comparison showed that the friction factor and Stanton-Prandtl moduli data deviated from the corresponding expressions by about ±20 and ±15 percent, respectively, suggesting the analysis to be largely correct. Reasonable agreement between the experimental data for the helical vane-without-centerbody and the wire-wrapped plugs and predictions was also obtained.

The analysis for pressure losses in helical-vane inserts was extended to the twisted-tape insert. Data obtained from the literature were compared with plain-tube expressions for friction factor and heat-transfer that were modified, in accordance with the analysis, for the twisted tape. This comparison suggested that the gross performance of the twisted tape can be predicted by the analysis.

*Nuclear Systems Programs, General Electric Co., Cincinnati, Ohio.

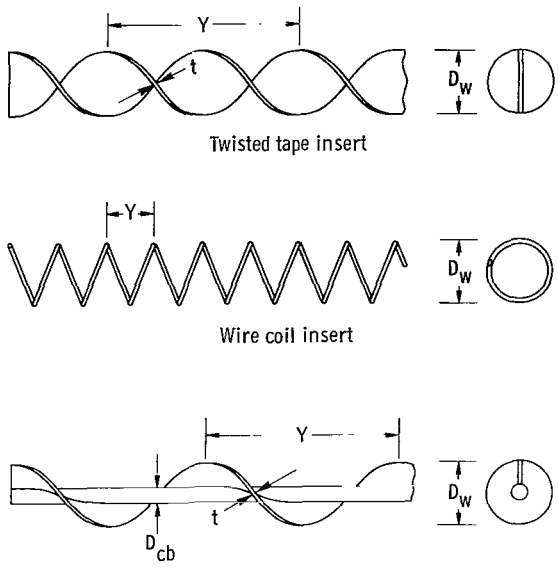

Figure 1. - Twisted tape, wire coil, and helical vane inserts.

INTRODUCTION

The use of swirl-generating inserts has long been recognized as a means of increasing the heat transfer to single-phase fluids flowing inside tubes. These inserts, such as the twisted tape, the helical wire coil, and the helical vane (fig. 1) promote the heat transfer by creating higher fluid velocities near the tube wall than would occur in linear flow through a plain tube.

More recently, swirl-generating inserts have been employed inside the tubes of liquid-metal boilers for space Rankine-cycle electric powerplants. Swirl inserts are considered beneficial for use in these boilers since they develop within the fluid an acceleration normal to the tube wall. This acceleration tends to separate the phases. The liquid, the more dense phase, is generally forced to flow toward and along the tube wall, thus delaying the onset of the dry-wall condition (refs. 1 and 2). Changes in boiler performance due to variations of the gravitational environment are believed to be minimized through the use of these inserts. Moreover, substantial reductions in the length of the superheat (all vapor) regions of these boilers are made possible by these inserts by the increase in the single-phase heat-transfer coefficients cited previously. The inserts (fig. 1) may be classified as thermally passive devices. They are fabricated to slip into a tube with a small clearance such that the contact areas between the insert and the tube wall are small and randomly located. The better heat-transfer performance observed with swirl-generating inserts is therefore largely due to the rotational velocity

imparted to the fluid; the fin-conduction effect is generally small, hence the term thermally passive.

A portion of most liquid-metal boilers is devoted to superheating the vapor, that is, the process of forced-convection heat transfer to a single-phase fluid. To design such boilers, correlations or methods to predict single-phase heat-transfer coefficients and pressure losses in tubes with inserts are required (ref. 3). In addition, a better knowledge of the single-phase performance of swirl inserts is considered important to provide bases for evaluating, correlating, and understanding their two-phase performance. To an extent, this information is available for the twisted-tape and wire coil. For example, references 4 to 9 report experimentally determined friction factors or heat-transfer coefficients for tubes containing twisted tapes in the range of pitch to tube diameter ratios of 3.6 to infinity. Reference 10 presents similar data for wire coils of pitch to tube diameter ratios between 0.046 and 5.3. References 4, 5, and 8 obtained correlations of twisted-tape friction factors or heat-transfer coefficients.

Limitations to the twisted tape and wire coil are evident from the references just cited. The twisted tape cannot be conveniently fabricated at pitch to tube diameter ratios below about three without structurally failing the metal strip (refs. 4 and 5). The heat-transfer performance of the wire coil decreases substantially at pitch-tube diameter ratios below about 0.5 (ref. 10). This decrease has been attributed to a bypassing of the heat-transfer surface by a portion of the fluid flowing in the insert.

The helical-vane insert, consisting typically of a single vane wrapped about and permanently attached to a supporting rod or centerbody, has several advantages. In a tube, this insert, in contradistinction to the twisted tape or wire coil, creates a single helical flow passage that is both physically and mathematically well defined. Fluid maldistribution between the two flow passages formed in a tube by the twisted tape, as has been observed by the authors, cannot occur with the helical vane. Substantial bypassing, which is indicated by the heat-transfer data for the wire coil, likewise is not possible for this insert; the bulk of the flow must follow the helical passage formed by the insert. Consequently, more reliable predictions and extrapolations of the thermal and hydraulic performance of the helical-vane insert can be expected.

In practical terms, the hollow centerbody of a helical vane insert provides a convenient location for instrumentation, such as thermocouples or pressure taps, that does not disturb the flowing fluid. For application of inserts to fluids that are highly corrosive or reactive, such as the liquid metals, this feature is important. Simple techniques are available that permit the fabrication of helical-vane inserts with pitch to tube diameter ratios as small as 0.5 (ref. 11, e.g.), a characteristic which permits optimization for any application. The centerbody structure is not required for the support of the vane. In fact, helical-vane inserts have been made without centerbodies in which the vane extended either a portion of or the full tube radius. The two main disadvantages of the

helical-vane insert, on the other hand, include a more complex fabrication than either the twisted tape or the wire coil and the possibly greater mass of this insert compared with the wire coil, both of which are reflected in higher cost. Finally, in applications such as boilers, secondary flows created by the swirl cause some liquid to flow along the insert structure. This effect is usually undesirable since the liquid on the insert bypasses the tube wall. All the swirl-generating inserts discussed herein are subject to this phenomenon.

Previous experimental studies of the helical-vane insert have been few. Reference 8 described the results of single-phase pressure loss and heat-transfer tests[1] of three helical-vane inserts having pitch to tube diameter ratios of 0.56, 1.12, and 2.24. Reference 1 measured the friction factors of three such inserts having pitch to tube diameter ratios of 2 and 6. Reference 12 reported the results of analyses and experiments of single- and two-phase (boiling) flow in helical-vane inserts. This reference also included a photographic study of two-phase flow in this insert configuration. Because of the limited data available in the literature describing the single-phase performance of the helical vane, an analytical and experimental investigation of this insert was conducted. The analytical investigation was conducted to provide a theoretical basis for predicting the pressure losses and heat-transfer coefficients for flow in tubes containing helical-vane inserts from corresponding plain-tube data. The analysis assumed solid-body rotation and employed conservation of linear and angular momentums. The experimental investigation consisted of measuring the pressure losses and heat-transfer coefficients of four different, full-length helical-vane inserts in a 2.21 centimeter-inner-diameter tube. These tests were conducted over a Reynolds number range of about 30×10^3 to 300×10^3, with limited data obtained beyond this range. Friction factors and Stanton-Prandtl moduli computed from the data were compared with plain-tube expressions modified, in accordance with the analysis, for the helical-vane insert. A limited number of experimental data obtained with two insert geometries that were similar to the helical vane were also compared with the modified plain-tube expressions. The analysis was extended to the twisted-tape insert. Selected data from the literature for the twisted tape were compared with the predictions obtained from the analysis.

[1]Campbell, S. A.; Greene, N. D.; et al.: Sea Water Conversion Studies. Rep. ERR-SD-024, Convair Division, General Dynamics Corp., Oct. 27, 1960. (Available from DDC as AD-251720.)

ANALYSIS OF PRESSURE LOSSES IN TUBES CONTAINING HELICAL-VANE INSERTS

An analysis was conducted to provide a theoretical basis for the prediction of pressure losses in tubes containing helical vane inserts. Definitions of symbols used in the equations are given in appendix A. The details of this analysis are presented in appendix B. The following paragraphs outline the approach taken and discuss the results which were obtained.

The fluid which passes through a tube into which a helical vane has been placed was assumed to rotate around the tube axis with a constant angular speed, that is, solid-body rotation. (The validity of this assumption has been experimentally demonstrated for twisted tapes by the authors of ref. 4) A further assumption was that helical streamlines within this fluid are parallel to the vane of the insert (i. e., secondary flows are neglected). Consequently, the analysis was predicated on fully developed, steady flow. By virtue of these assumptions, the fluid helical velocity V_h was resolved into an axial component V_z and a tangential velocity V_θ as shown in figure 2. The axial velocity was obtained from continuity. The tangential and helical velocities were related to the

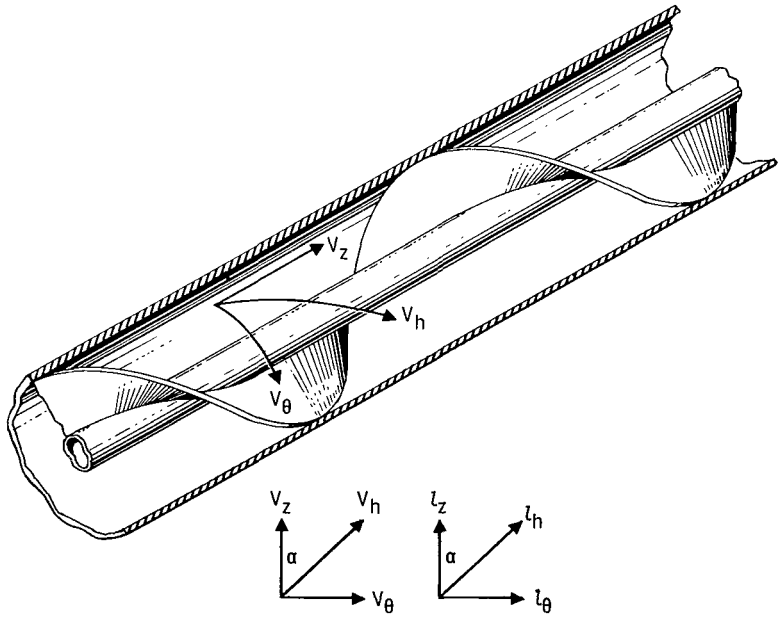

Figure 2. - Resolution of fluid helical velocity into axial and tangential components.

axial velocity by the geometry of the insert and both were functions of the radial displacement from the tube centerline. The equations relating V_z, V_θ, and V_h are

$$V_z = \frac{m}{A_c \rho} \tag{1}$$

$$V_\theta = \left(\frac{2\pi r}{Y}\right) V_z = \left(\frac{l_\theta}{l_z}\right) V_z \tag{2}$$

$$V_h = \left\{ \frac{\left[Y^2 + (2\pi r)^2\right]^{1/2}}{Y} V_z \right\} = \left(\frac{l_h}{l_z}\right) V_z \tag{3}$$

$$V_h = \left(V_z^2 + V_\theta^2\right)^{1/2} \tag{4}$$

The cross-sectional area for flow A_c required for calculation of the axial velocity is given by

$$A_c = \pi \left(r_w^2 - r_{cb}^2\right) - \int_{r_{cb}}^{r_w} t \left(\frac{l_h}{l_z}\right) dr \tag{5}$$

The maximum helical velocity occurs at the tube radius r_w as shown in the following equation:

$$V_{h,w} = \left\{ \frac{\left[Y^2 + (2\pi r_w)^2\right]^{1/2}}{Y} V_z \right\} = \left(\frac{l_{h,w}}{l_z}\right) V_z \tag{6}$$

Using the preceding expressions for the velocity distribution within a tube containing a helical-vane insert, conservation of linear and angular momentums was applied to a control volume of the fluid. The two equations that were obtained were solved for a single expression for the pressure loss across an axial increment of a tube containing a helical-vane insert. This equation consisted of separable momentum and frictional pressure-loss terms. The momentum pressure-loss term, as derived from this analysis, was

$$\Delta P_{m,h} = \frac{m^2}{A_c^2}\left(\frac{1}{\rho_e} - \frac{1}{\rho_i}\right)\left[1 + \frac{2\pi^3}{Y^2}\frac{\left(r_w^4 - r_{cb}^4\right)}{A_c}\right] \tag{7}$$

And the frictional pressure-loss term was

$$\Delta P_{f,h} = f_h \frac{l_z}{D_h}\left(\frac{l_{h,w}}{l_z}\right)^3\left[\bar{\rho}\frac{\bar{V}_z^2}{2}\right] \tag{8}$$

By assuming the equality of friction factors at the tube wall, insert vane, and centerbody, the hydraulic diameter was derived as

$$D_h = \frac{4A_c}{p_w + \left(\frac{l_{h,cb}}{l_{h,w}}\right)^3 p_{cb} + 2\left(\frac{l_z}{l_{h,w}}\right)^3 \int_{r_{cb}}^{r_w} \left(\frac{l_h}{l_z}\right)^4 dr} \tag{9}$$

The terms p_w and p_{cb} were the wetted perimeters of the tube wall and centerbody, respectively. Equation (8), defining the helical-vane-insert friction factor, may be rewritten by substitution of equation (6). This alternate expression is shown below after rearrangement:

$$f_h = \frac{\Delta P_{f,h}}{\left(\frac{l_{h,w}}{D_h}\right)\left(\bar{\rho}\frac{\bar{V}_{h,w}^2}{2}\right)} \tag{10}$$

Equation (10) evaluates the friction factor employing both the maximum helical velocity, which occurs near the tube wall, and the maximum helical path length. Moreover, the equivalent hydraulic diameter used in equation (10) differs from the conventional expression in that the wetted perimeters of the tube wall, vane, and centerbody surfaces are weighted in accordance with the fluid helical velocities adjacent to these surfaces. The form of equation (10), however, is identical to the usual expression for friction factor in

a plain tube. Consequently, by analogy, the Reynolds number for flow in a tube with a helical-vane insert was defined as

$$Re_h = \left(D_h \bar{V}_{h,w} \frac{\bar{\rho}}{\bar{\mu}}\right) = \left(D_h \bar{V}_z \frac{l_{h,w}}{l_z} \frac{\bar{\rho}}{\bar{\mu}}\right) \tag{11}$$

Equations (10) and (11) imply that helical-vane-insert friction factors might be correlated by a conventional expression for friction factors $\left(\text{e.g., } f_o = 0.184\ Re_o^{-0.2}\right)$ in which the helical parameters of f_h and Re_h are substituted for those of the plain tube.

Reference 5 attempted to correlate twisted-tape friction factors in accordance with the equation

$$f_t = \frac{\Delta P_t}{\left(\frac{l_{h,w}}{D_e}\right)\left(\bar{\rho} \frac{\bar{V}_{h,w}^2}{2}\right)} \tag{12}$$

Reference 12 likewise employed a form of equation (12) to correlate twisted-tape and helical-vane friction factors. With the exception of the diameter term, equation (12) is identical with equation (10) which was derived from conservation of momentum. Consequently, the use of an equation having the form of equation (12) is given a theoretical basis by the analysis presented herein. Reference 5 assumed an equivalent diameter for use in equation (12) calculated from the conventional hydraulic diameter, that is, four times the ratio of the flow cross-sectional area perpendicular to the tube axis divided by the total wetted perimeter. References 6 and 12 assumed an equivalent diameter based on the mean flow area normal to the helical streamlines and the corresponding mean perimeter. Equation (9), which presents the hydraulic diameter for helical-flow inserts, is not an assumed equation, but a quantity derived from the same conservation analysis used to obtain the momentum and frictional pressure losses (eqs. (7) and (8)). For the inserts of this investigation, the theoretically based equivalent diameters were as much as 20 percent larger than those computed from the conventional definition of hydraulic diameter.

EXPERIMENTAL APPARATUS

The apparatus used in the experiments is shown schematically in figure 3. Air from the supply flowed through a pressure regulator, a standard ASME metering orifice, an

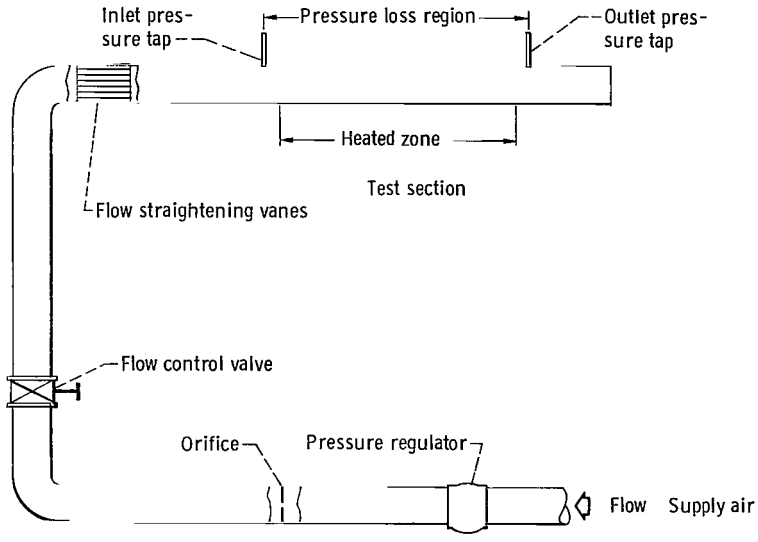

Figure 3. - Schematic diagram of test apparatus.

air-control valve, and a flow straightener before entering the test section. The length of straight tubing between the flow straightening vanes and the upstream pressure tap was 97 centimeters. Orifice pressure differences were determined by a 1.52-meter water manometer subdivided to 0.25 centimeter. Orifice inlet pressures were measured with a calibrated Bourdon tube gage subdivided to 1.27 centimeters of Hg. Several different metering orifice plates having orifice diameters ranging from 0.19 to 2.03 centimeters were employed to cover the desired flow rate range.

Figure 4 is a schematic of the test section. The test section was constructed from a 1.96-meter length of 2.54-centimeter outside-diameter stainless steel (AISI 316) tubing having a wall thickness of 1.65 millimeters. The inside diameter of the tube was measured to a depth of about 13 centimeters at the inlet and exit using an internal micrometer. The tube inside diameter was determined in this manner as 2.210±0.003 centimeters. Because the measurements were made only at the ends of the test section, the uncertainty in tube diameter was estimated as ±0.005 centimeter. Two pressure taps were positioned 1.118±0.003 meters apart with the downstream tap located 12.7 centimeters from the end of the test section. The inserts tested extended typically over a 1.83-meter length of the test section thereby providing 58.5 centimeters of flow development length before the upstream pressure tap. The pressure taps were constructed by welding 0.64-centimeter outside-diameter tubing to the test section over 0.076-centimeter-diameter pressure tap holes. The inside of the test section was carefully polished in the vicinity of the taps to insure the absence of burrs.

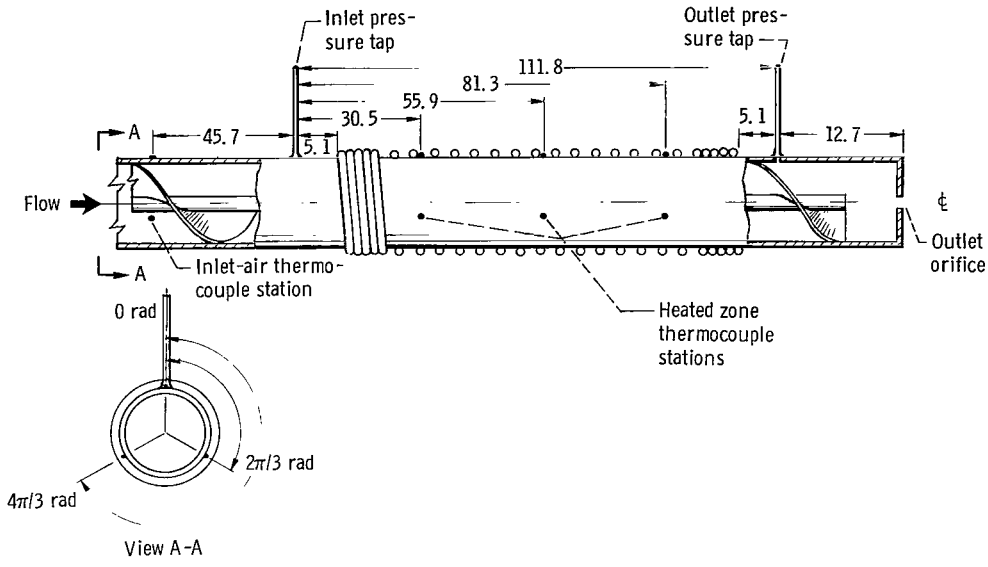

Figure 4. - Schematic of test section. Tube outer diameter, 2.54 centimeters; tube wall thickness, 1.65 centimeters; distance between inlet straightening vanes and inlet pressure tap, 97 centimeters.

A 76-centimeter water manometer and a 2.54-meter mercury manometer, both subdivided to 0.25 centimeter, were used to measure test section pressure loss. A valving arrangement was provided to shut off the water manometer when its range was exceeded. Differentials as low as 5 centimeters were recorded, but the readings were generally above 25 centimeters. Test-section exit pressure was measured with a 76-centimeter mercury manometer also subdivided to 0.25 centimeter. For some of the tests, orifices having diameters between 0.5 and 2.0 centimeters were placed at the outlet end of the test section. The purpose of these outlet orifices was to operate the test section at relatively high average pressure levels. This kept the momentum pressure losses small relative to the frictional losses.

The test section was heated over a 1.016±0.003-meter length located symmetrically between the pressure taps. This was accomplished by wrapping the stainless steel tube with 15.25 meters of 0.25-centimeter-diameter sheathed heating wire. This heating wire was held in place by strips of metal foil that were tack-welded to the tube wall. The turns of the heating wire were uniformly spaced 0.64 centimeter apart except for six turns at each end where the spacing was halved to minimize temperature gradients due to axial heat-conduction losses. Assembly of the test section was completed by application of a 0.64-centimeter-thick layer of high conductivity, graphite-base refractory cement to embed the heating wires followed by a 5.1-centimeter-thick layer of thermal insulation. Electrical power inputs of up to 4 kilowatts were attained with this arrangement, corresponding to heat fluxes of up to 56 700 watts per square meter. Figure 5 is a photograph of the test section prior to application of the refractory cement.

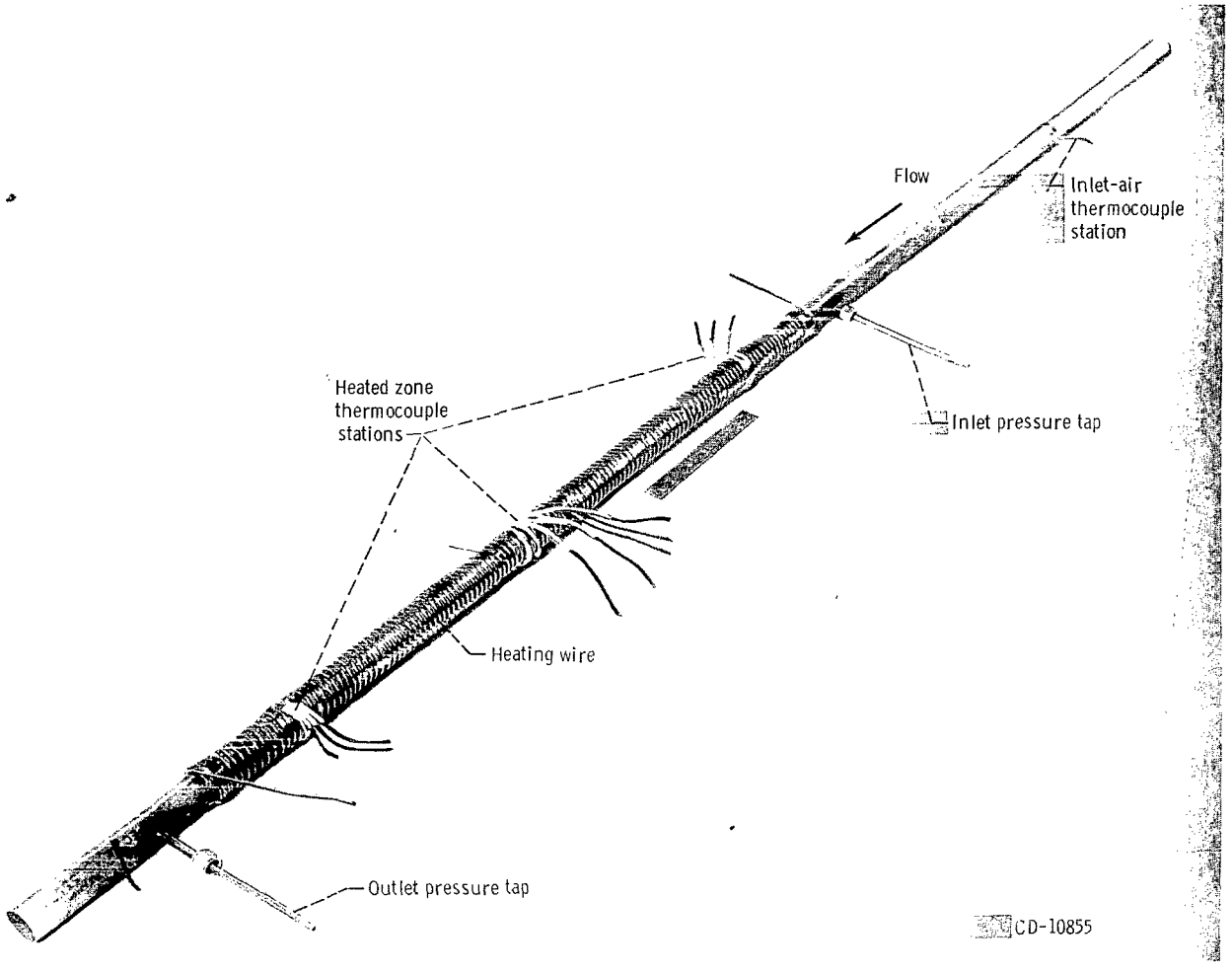

Figure 5. - Test section before insulation.

Four thermocouple stations were provided on the test section: one to determine inlet-air temperature and three to measure local wall temperature in the heated zone. Each station consisted of three Chromel-Alumel thermocouples that were tack-welded to the tube wall and positioned uniformly around the tube circumference. The thermocouple leads were wrapped around the tube three times before penetrating the thermal insulation in order to avoid lead conduction error. Both the thermocouple junctions and the leads wrapped around the tube were embedded in refractory cement in the heated zone. The inlet-air thermocouple station was located 51 centimeters upstream of the start of the heated zone to avoid errors due to axial conduction along the tube wall and was thermally insulated. The three heated-zone thermocouple stations were located equidistant from each other and from the ends of the heated zone. Each thermocouple was provided with an individual ice-bath reference junction.

Initially, a series of tests was conducted with the test section without an insert. These plain-tube tests consisted of the measurement of nonadiabatic pressure losses and heat-transfer coefficients and had the purpose of assuring the accuracy of the instrumentation and data reduction procedures. Subsequently, pressure-loss and heat-transfer tests were conducted with the test section containing helical-vane inserts. The insert pressure losses were measured both with and without heat addition to the test section. Four full-length helical-vane inserts having pitch to tube diameter ratios Y/D_w of 0.52, 0.75, 1.46, and 6.36 were tested. The inserts having Y/D_w of 0.52, 0.75, and 1.46 were machined out of brass. The $Y/D_w = 6.36$ insert was fabricated by stretching out split stainless-steel washers along the centerbody and welding the washers together and to the centerbody. The nominal diameter of the centerbody of these inserts was 0.6 centimeter, and the vane thicknesses ranged between 0.086 and 0.185 centimeter. The maximum radial clearance between the outer edge of the helical vanes and the tube wall was determined to be 0.0075 centimeter. Based on the largest pressure gradient employed in the tests, it was estimated that only about 1 percent of the total flow could pass through this maximum clearance gap between the insert and tube wall. Table I presents the average pitch (axial distance traversed for a 360^o revolution of the vane), centerbody diameter, vane thickness, and the standard deviation of these dimensions calculated from the measurements for the four inserts that were tested. Table I also includes the values of D_h computed from equation (9) for the four inserts and the ratio of D_h to the conventional hydraulic diameter D_e (defined as four times the flow cross-sectional area divided by the wetted perimeter).

EXPERIMENTAL PROCEDURES AND ERROR ANALYSIS

Before the start of testing, test-section heat losses were experimentally measured. Both ends of the tube were plugged, and the wall temperature was measured as a function of the power input. This information was then used to correct subsequent data for heat losses. An additional correction was made for the losses from the test-section heating wire to the power-cable connections. The largest heat-loss correction was 100 watts, and the correction for losses from the heating wire not in contact with the test section was about 4 percent of the input power.

All test-section thermocouples were intercalibrated in place before testing. Calibrations were obtained at ambient temperature and at about 373 K by flowing both air and saturated steam through the apparatus at low velocity. The calibration data showed the thermocouples to agree among themselves and with standard conversion tables within a maximum error of 0.3 K. This error was accepted; the thermocouples were used without correction thereafter.

The procedures employed to take experimental data were designed to maximize accuracies. Thus, the data were obtained as a function of air flow rate, proceeding from low flow rates to high. Data were overlapped when the metering orifice plates were changed, that is, whenever the orifice pressure differential fell below 25 centimeters of water. Accuracy in the measurement of heat-transfer coefficients is attained in the apparatus by maintaining a relatively large tube-wall- to bulk-air-temperature difference. Likewise, since bulk-air temperatures at locations corresponding to the wall thermocouple stations were calculated from a heat balance, accuracy is also achieved by minimizing the temperature change of the air flowing through the test section. Consequently, test section power was adjusted to maintain the tube-wall- to bulk-air-temperature difference generally above 38 K and always above 14 K, and the bulk-air temperature rise was generally kept below 56 K. Data were recorded when thermal equilibrium was attained as indicated by the constancy of test-section wall thermocouples. The approach to equilibrium required 1 to 2 hours. Air flow rates were calculated from the standard orifice equation using a compressibility factor of 1.0 and an orifice discharge coefficient of 0.61. The maximum orifice pressure differential was 0.15×10^5 newtons per square meter as compared with an orifice upstream pressure of 7×10^5 newtons per square meter, thus eliminating compressibility as a consideration. The orifice Reynolds number was always in the range where the discharge coefficient is relatively constant. The accuracy of the flow measurement, therefore, is estimated at 2 percent (based on ref. 13).

Bulk-air temperatures at test-section locations corresponding to the three wall thermocouple stations were calculated by a heat balance that assumed uniform heat addition as follows: The inlet-air station thermocouples were assumed to measure adiabatic wall temperatures. The three thermocouple readings were averaged and converted to a total temperature using the air velocity at this station and a recovery factor of 0.85 (ref. 14). The change in total temperature of the air was then calculated from the heat input and the air flow rate and was added to the inlet total temperature. This total temperature was then converted to an adiabatic wall temperature using the local air velocity and the same value of the recovery factor. These corrections were very small except at the highest flow rates. The bulk air properties, including density, viscosity, and thermal conductivity, were evaluated at the local static temperature, which was calculated from the corresponding local total temperature.

The thermocouple stations in the heated zone were assumed to measure the outer wall temperature of the test section. At any one thermocouple station, the temperature readings between thermocouples differed typically by about 8 K, corresponding to an approximately 15-percent circumferential variation in heat-transfer coefficient. This variation in the coefficient appeared to be real. The three thermocouple readings at each station were therefore averaged, and this average temperature was employed to

calculate the inner wall temperature using a standard equation for the radial conduction of heat in hollow cylinders. The heat flux, required for the calculation of the inner wall temperature, was obtained by dividing the net power input by the heat-transfer area of the 1.016-meter-long heated zone, based on the inner diameter of the tube. The maximum temperature difference between the outer and inner walls of the tube computed in this manner was 5.5 K.

Heat-transfer coefficients determined at the first thermocouple station within the heated zone during tests with the plain tube (tube without an insert) were approximately 10 percent larger than those measured at the two other stations. This suggested the possibility of an entrance effect on the heat-transfer coefficients at this station. Consequently, the heat-transfer coefficients reported herein are based on measurements made at the central wall thermocouple station within the heated zone of the test section.

An error analysis was performed in order to determine the accuracies to be expected from the experiment. It was assumed for this analysis that the air flow rate calculated from the standard orifice had an accuracy of 2 percent, that individual temperature measurements were accurate to 0.6 K based on the calibration data, and that manometers could be read to 1/2 of the smallest division or 0.125 centimeter. The corrected power reading was assumed to have an accuracy of $1\frac{1}{2}$ percent, based on the wattmeter full-scale accuracy of 0.75 percent. The various basic errors were assumed to be independent and the method of reference 15 was employed to estimate the error of the pressure-loss and heat-transfer-coefficient determinations for an average case. The results are

Calculated error in pressure loss measurement, percent	0.5
Calculated error in heat-transfer coefficient, percent	2.0

Further error is introduced when the pressure loss data are reduced to the frictional and momentum pressure losses and then converted into friction factors. Likewise, additional error arises from the conversion of the heat-transfer coefficients to the Stanton-Prandtl moduli. The test-section tube diameter enters as the fifth power in calculation of the friction factor and as the second power in calculation of the Stanton-Prandtl modulus. Assuming the 0.005 centimeter uncertainty in tube diameter discussed earlier, the estimated errors are as follows:

Calculated friction factor error, percent	4.2
Calculated Stanton-Prandtl modulus error, percent	2.9
Calculated Reynolds number error, percent	2.0

Table II presents the estimated combined probable errors in the helical parameters of friction factor, Stanton number, and Reynolds number that arise from instrument inaccuracies and variations in the physical dimensions of the inserts tested. A large portion of the probable errors shown in this table are due to the variability of insert pitch with length which occurred during fabrication. This effect is especially true of the insert having the largest pitch to tube diameter ratio.

EXPERIMENTAL RESULTS

Figure 6 is a plot of the measured overall static-pressure loss as a function of air flow rate for the plain tube and for the same tube with the four helical-vane inserts. (The helical-vane-insert data were taken under adiabatic conditions.) The lines drawn through the data for the inserts tend to decrease in slope at the larger flow rates. This effect was due to the increase in air density with increased flow rate. A plot of the

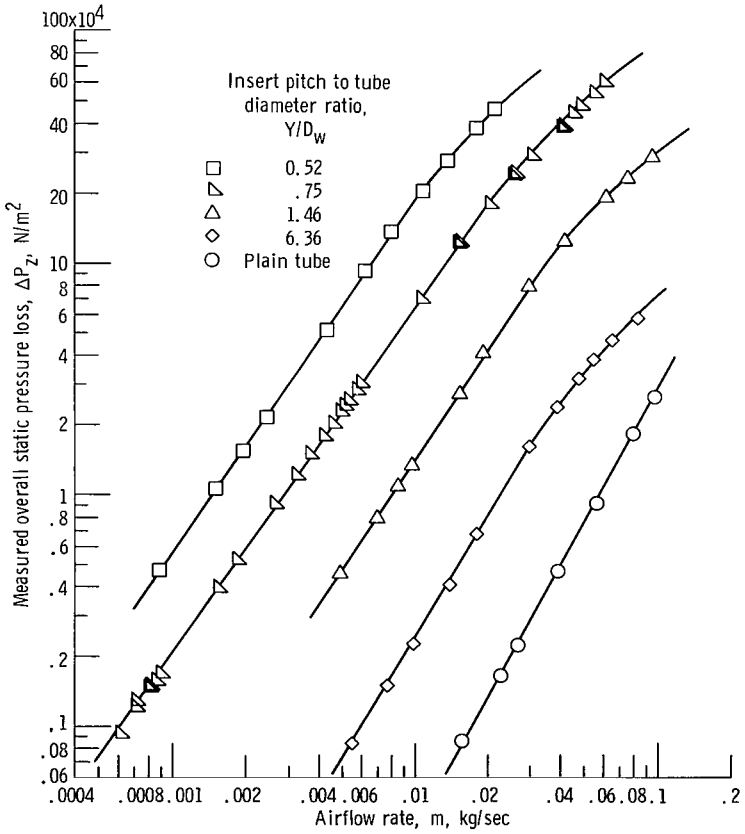

Figure 6. - Measured overall static-pressure loss for four helical-vane inserts and the plain tube.

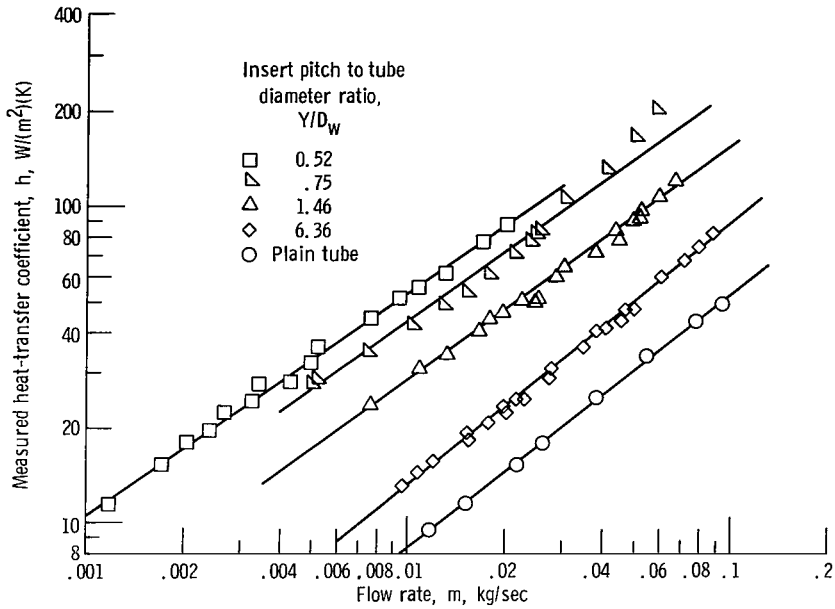

Figure 7. - Measured heat-transfer coefficient for four helical-vane inserts and the plain tube.

measured heat-transfer coefficients as a function of air flow rate for the same tube and inserts is shown in figure 7. Figures 6 and 7 illustrate that the pressure losses and heat-transfer coefficients increase with increased mass flow rate. Decreasing the insert pitch to tube diameter ratio Y/D_W results in substantial increases of the heat-transfer coefficient and the pressure loss. For example, the helical-vane insert with a pitch to tube diameter ratio of 0.52 developed heat-transfer coefficients that were approximately 3.8 times those of the $Y/D_W = 6.36$ insert. However, the corresponding overall static-pressure losses increased by a factor of about 60. Table III presents the experimental data obtained in this investigation.

DISCUSSION OF RESULTS

Frictional Pressure Losses and Heat Transfer in the Plain Tube

To validate the experimental techniques employed in the investigation, friction factors f_o and Stanton-Prandtl moduli J_o were computed from the plain tube data presented in figures 6 and 7. Conventional equations were employed in computing f_o and J_o.

The plain-tube friction factors are shown plotted against Reynolds number in figure 8(a). The following correlation of friction factors for smooth tubes (ref. 16) is

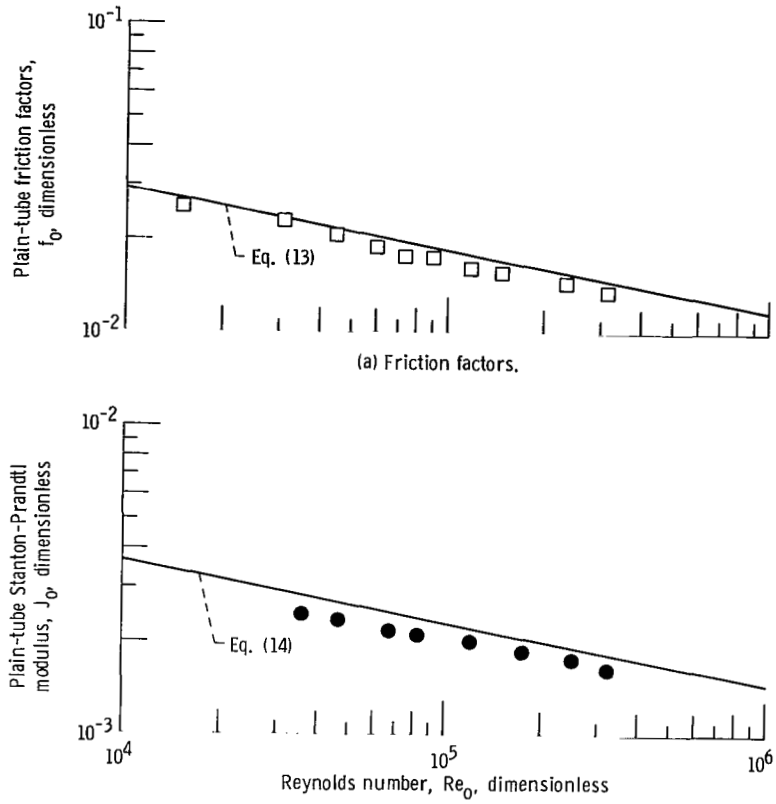

Figure 8. - Comparison of plain-tube experimental data with correlations.

shown plotted in the same figure for comparison.

$$f_o = \frac{0.184}{Re_o^{0.2}} \tag{13}$$

In the range of Reynolds numbers of about 30×10^3 to 300×10^3, the friction factor data of figure 8(a) fall approximately 10 percent below the line corresponding to equation (13). The Stanton-Prandtl moduli computed from the data are compared in figure 8(b) with the following equation for heat transfer in plain tubes (ref. 16):

$$J_o = (St_o)(Pr)^{0.6} = 0.023(Re_o)^{-0.2} \tag{14}$$

The experimental values of J_o in figure 8(b), likewise, fall about 10 percent below the correlating equation. The agreement of the f_o and J_o data and the lack of internal

scatter show the measurements and data reduction procedures to be adequately accurate and precise.

Correlation of Experimental Pressure-Loss Data for Tubes Containing Helical-Vane Inserts

The experimental overall static-pressure losses shown in figure 6 and the pressure-loss data obtained with heat addition were reduced in accordance with the equations derived from the analysis. Specifically, equation (7) was used to calculate the momentum pressure losses that occurred in the insert test sections. The momentum pressure losses were subtracted from the overall static-pressure losses to yield the frictional pressure losses $\Delta P_{f,h}$. An indication of the typical magnitudes of the computed momentum losses as a fraction of the frictional pressure losses can be seen in figure 9 for the tube containing the 1.46-pitch-to-tube-diameter-ratio insert. Both adiabatic and heat addition runs are shown plotted in this figure. The maximum value of the ratio $\Delta P_{m,h}/\Delta P_{f,h}$ was 0.35, which occurred with heat addition to the test section.

Friction factors and corresponding Reynolds numbers were computed from the data by application of equations (10) and (11). Figure 10 is a plot of the data so reduced for

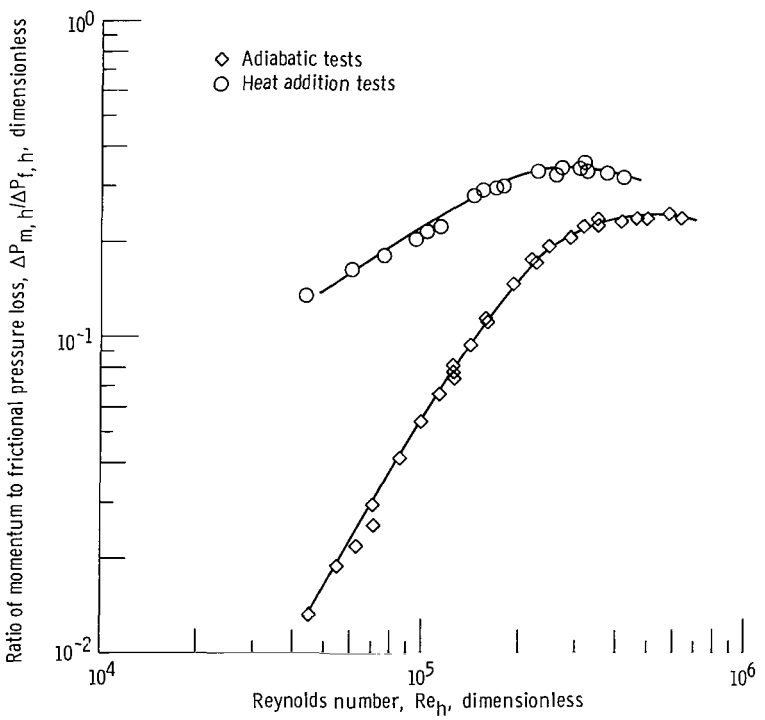

Figure 9. - Typical magnitude of momentum pressure losses. Insert pitch to tube diameter ratio, 1.46.

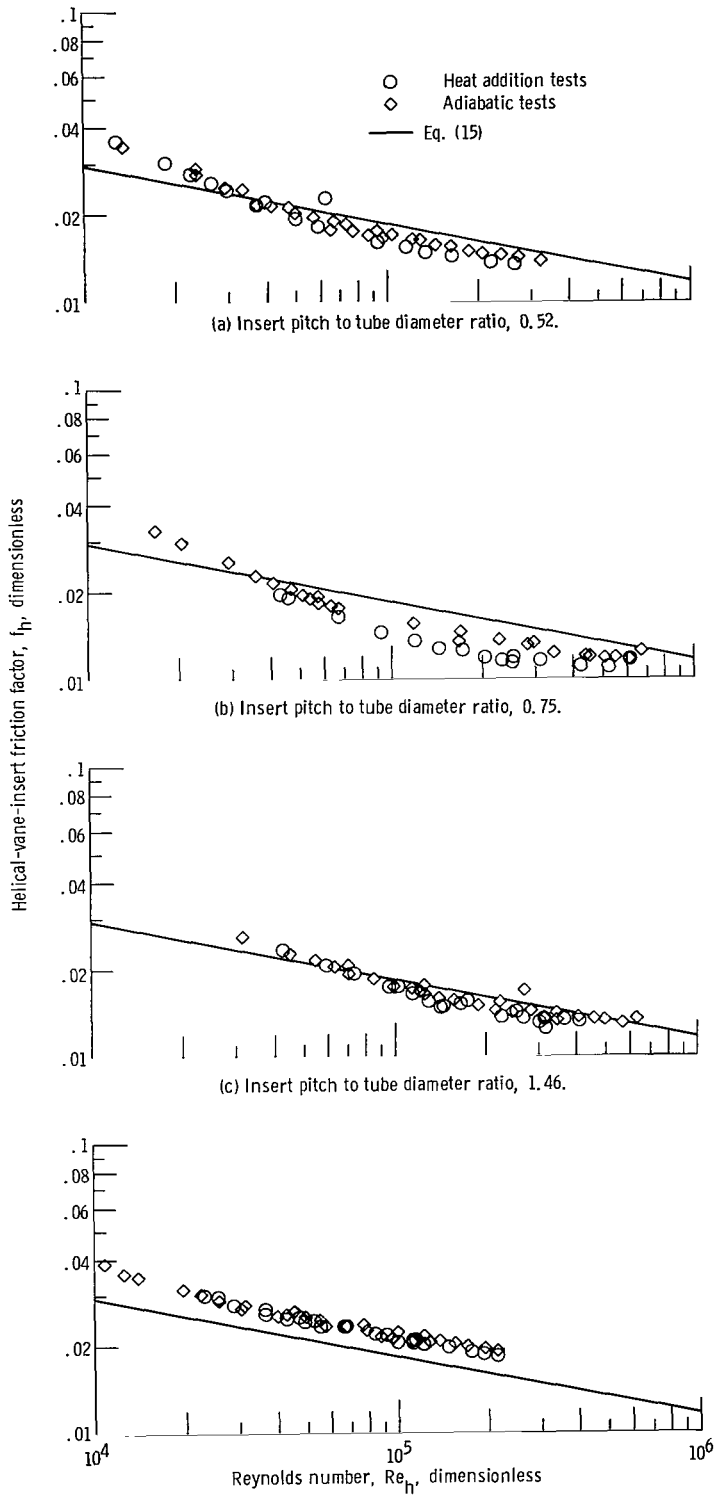

(a) Insert pitch to tube diameter ratio, 0.52.

(b) Insert pitch to tube diameter ratio, 0.75.

(c) Insert pitch to tube diameter ratio, 1.46.

(d) Insert pitch to tube diameter ratio, 6.36.

Figure 10. - Comparison of helical-vane-insert friction factors with correlating equation.

the four helical-vane inserts that were tested. Equation (13), modified for the helical-vane insert, may be written as

$$f_h = \frac{0.184}{Re_h^{0.2}} \tag{15}$$

Equation (15) is plotted as a line in figure 10. The friction factor data shown in this figure appear to exhibit a trend with Reynolds number somewhat different from that of equation (15); that is, an average line drawn through the data would decrease rapidly at low Reynolds numbers and level off or increase slightly at the higher Reynolds numbers. This characteristic is believed to be real, but its explanation is unknown. In the range of Reynolds numbers of 30×10^3 to 300×10^3, of the more than 130 data points shown in figure 10, only about 10 percent deviated more than ±20 percent from the line corresponding to equation (15). This agreement suggests that the assumption of solid-body rotation, as made in the analysis presented herein, is largely correct. Secondary flows, known to occur in fluids passing through swirl-generating inserts such as twisted tapes, are not accounted for in the analysis. The deviations of the friction factor data from the correlation, as described previously and shown in figure 10, may therefore be due in part to this phenomenon.

Correlation of Experimental Heat-Transfer Coefficients for Tubes Containing Helical-Vane Inserts

The measured heat-transfer coefficients and the flow rates of air were reduced to Stanton-Prandtl moduli and Reynolds numbers modified for helical flow. These parameters were defined as follows:

$$J_h = St_h Pr^{0.6} = \left[\frac{h}{C_p \rho V_z \left(\frac{l_{h,w}}{l_z}\right)}\right]\left(\frac{C_p \mu}{k}\right)^{0.6} \tag{16}$$

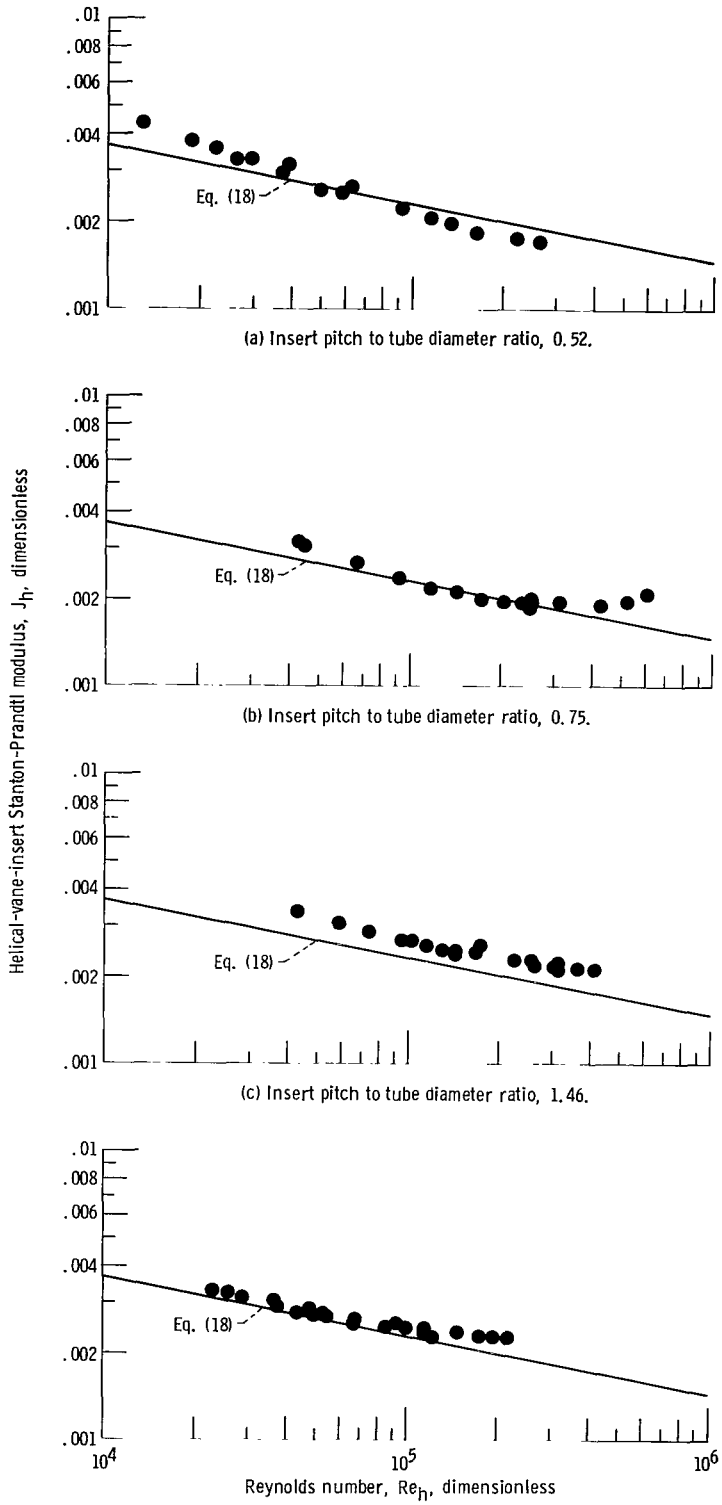

(a) Insert pitch to tube diameter ratio, 0.52.

(b) Insert pitch to tube diameter ratio, 0.75.

(c) Insert pitch to tube diameter ratio, 1.46.

(d) Insert pitch to tube diameter ratio, 6.36.

Figure 11. - Comparison of helical-vane-insert Stanton-Prandtl moduli with correlating equation.

$$Re_h = \left[\frac{D_h V_z \left(\frac{l_{h,w}}{l_z} \right) \rho}{\mu} \right] \tag{17}$$

It should be noted that equation (17) differs from equation (11) in that local rather than average physical properties of the fluid are employed. Likewise, equation (16) employs local fluid properties. The use of local properties is appropriate since circumferential average heat-transfer coefficients at a single axial station were determined.

Figure 11 presents the experimental values of J_h as a function of Re_h for the four helical vane inserts. The following equation is shown plotted in the same figure:

$$J_h = 0.023(Re_h)^{-0.2} \tag{18}$$

The selection of equation (18) for comparison with the experimental heat-transfer data, including the use of the hydraulic diameter D_h given by equation (9), which is implicit in equation (18), was justified by the Colburn analogy (ref. 17) and the success in correlating the helical-vane-insert friction factors. This analogy asserts the similarity of thermal and hydraulic boundary layers thus providing a basis for predicting heat transfer from hydraulic phenomena.

In general, the Stanton-Prandtl modulus data presented in figure 11 seem to exhibit a trend with Reynolds number similar to that of the friction factor data of figure 10: a line through the data would tend to reach a minimum or even increase at the higher Reynolds numbers. As with the friction factors, the causes of this effect are unknown. Nevertheless, of the 56 data points in the range of Reynolds numbers between 30×10^3 and 300×10^3, only about 5 percent deviated more than ±15 percent from equation (18). Figure 11, therefore, indicates that the momentum analysis can reasonably predict heat-transfer coefficients for flow inside tubes containing helical-vane inserts.

Application of equation (18) is limited to passive helical-vane inserts of the type reported herein. For helical inserts in which the vane makes good thermal contact with the tube wall, an appropriate expression accounting for the fin conduction effect must be formulated.

COMPARISONS WITH AXIAL FLOW MODEL

Previous investigators have frequently reported experimentally determined fric-

tion factors and heat-transfer data of swirl-generating inserts on the basis of an axial flow model. In this model, the friction factor, Reynolds number, and Stanton-Prandtl modulus are defined as follows:

$$f_A = \frac{\Delta P_{f,h}}{\frac{l_z}{D_w}\rho\frac{V_z^2}{2}} \tag{19}$$

$$Re_A = \frac{D_w V_z \rho}{\mu} \tag{20}$$

$$J_A = \left(\frac{h}{C_p \rho V_z}\right)\left(\frac{C_p \mu}{k}\right)^{0.6} \tag{21}$$

Values of f_A and J_A as a function of Re_A for tubes containing helical-vane inserts have been reported, as indicated in the INTRODUCTION to this report, in references 8 and 1. In particular, reference 8 presented lines corresponding to the best fit of axial friction factors (measured by Greene) for helical-vane inserts having pitch to tube diameter ratios of 0.56, 1.12, and 2.24 contained in a 2.26-centimeter-diameter tube. This reference also presented heat-transfer data for the same inserts in a form corresponding to J_A/J_o. Figure 12 reproduces the lines of reference 8 with the exception that the insert friction factors f_A were normalized by the authors of this report to plain tube values f_o using equation (13). Figure 12(a) also contains f_A data obtained by reference 1 (and subsequently normalized to f_o) for two helical-vane inserts having pitch to tube diameter ratios of 2.0 and 6.0 and contained inside a 2.34-centimeter-diameter tube. Figure 12 indicates that f_A and J_A are strongly dependent on the pitch to tube diameter ratio and vary somewhat with Reynolds number Re_A.

Equations (15) and (18), inferred from the analysis of this report and used to correlate the helical parameters of f_h and J_h, were modified to predict the ratios f_A/f_o and J_A/J_o. The derivation of the equations to predict the normalized friction factors and Stanton-Prandtl moduli is presented in appendix C; the results are

$$\frac{f_A}{f_o} = \left(\frac{D_w}{D_h}\right)^{1.2}\left(\frac{l_{h,w}}{l_z}\right)^{2.8} \tag{22}$$

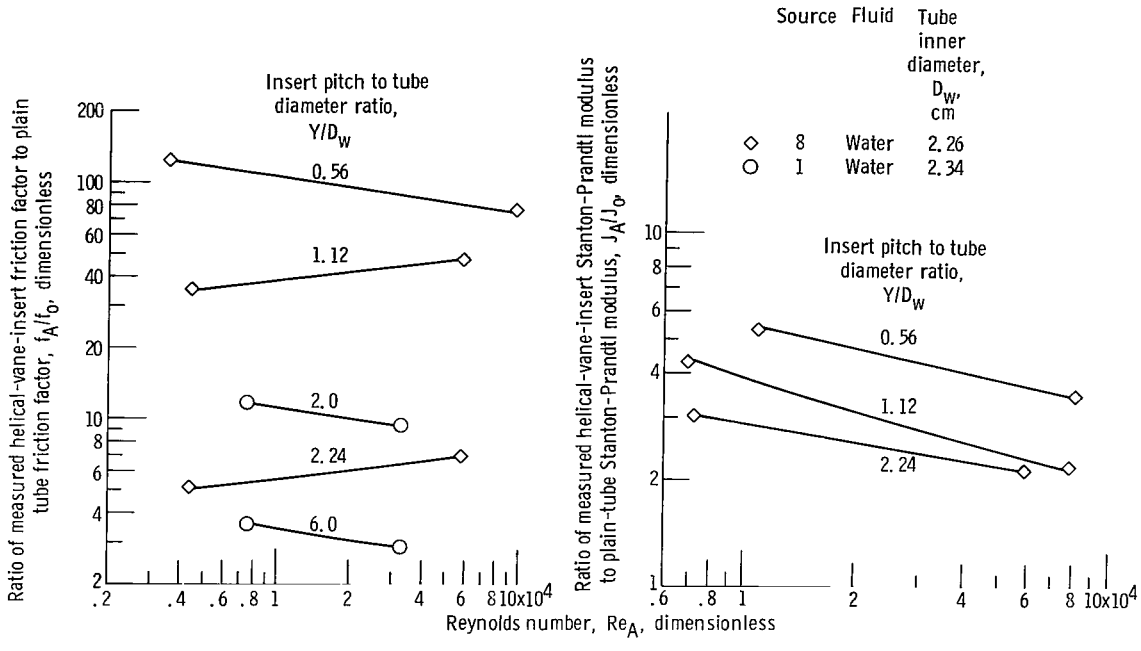

(a) Friction factors of references 1 and 8.

(b) Stanton-Prandtl moduli of reference 8.

Figure 12. - Normalized helical-vane-insert parameters reported by other investigators.

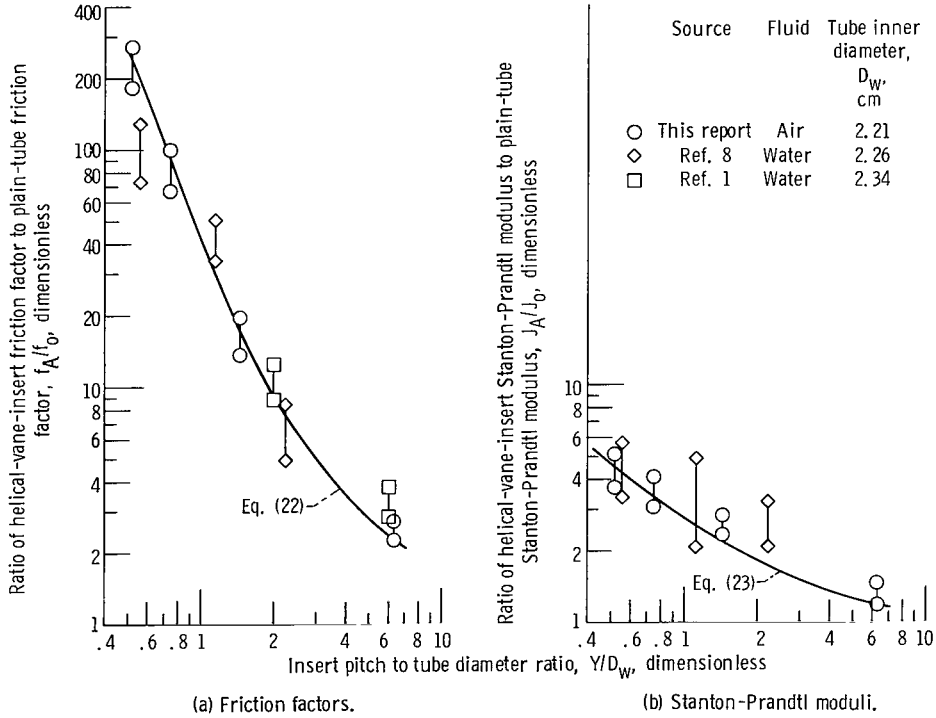

(a) Friction factors.

(b) Stanton-Prandtl moduli.

Figure 13. - Comparison of experimental normalized helical-vane-insert parameters with theory.

$$\frac{J_A}{J_o} = \left(\frac{D_w}{D_h}\right)^{0.2} \left(\frac{l_{h,w}}{l_z}\right)^{0.8} \tag{23}$$

Equations (22) and (23), which are independent of Reynolds number, are plotted as a function of pitch to tube diameter ratio in figure 13, using values of D_w and D_{cb}/D_w of the inserts of this report. In addition, plotted on these figures are the range of f_A/f_o and J_A/J_o of figure 12 and the ranges of the same parameters for the four helical-vane inserts reported herein. (Ref. 18 presents a graph of f_A as a function of Re_A for the inserts of this study.) Figure 13 suggests that the gross trends of f_A/f_o and J_A/J_o, as predicted by equations (22) and (23), are confirmed by the data. Moreover, most of the data used to prepare these figures appear to fall within about ±20 percent of the predicted lines. The maximum deviation of the normalized friction factors, occurring with the $Y/D_w = 1.12$ insert, is about +60 percent. The maximum deviation of the normalized Stanton-Prandtl moduli data from the predicted curve is +75 percent occurring with the $Y/D_w = 2.24$ insert. All the normalized friction-factor and Stanton-Prandtl moduli data exhibit variations with Reynolds number. In general, the deviations from the predicted curves may be due to secondary flows, fin conduction, surface roughness, or combinations of these effects.

Figure 13 provides a summary of the heat-transfer enhancement and frictional pressure-loss penalty associated with the use of helical-vane inserts. Moreover, graphs of the type shown in these figures can be used to facilitate the evaluation of these inserts for particular applications. Thus, the designer need only compute the values of f_o and J_o for his application and multiply these by corresponding ratios, shown, for example, in the figures, to obtain an estimate of the performance of the helical-vane insert. Momentum pressure losses, entrance- and exit-pressure losses, and entrance effects on heat-transfer coefficients would have to be considered as well in a detailed design.

APPLICATION TO INSERTS OF SIMILAR GEOMETRY

A limited amount of testing was conducted with swirl-generating inserts having geometrical similarity to the helical-vane insert. These inserts were a helical vane-without-centerbody and a wire-wrapped plug. The plug insert consists of a relatively large centerbody around which a single helical wire is wrapped. Sketches of both of these inserts are shown in figure 14. The data obtained from these experiments were reduced using the equations derived for the helical-vane insert. The resultant friction factors and Stanton-Prandtl moduli were compared with the corresponding correlating

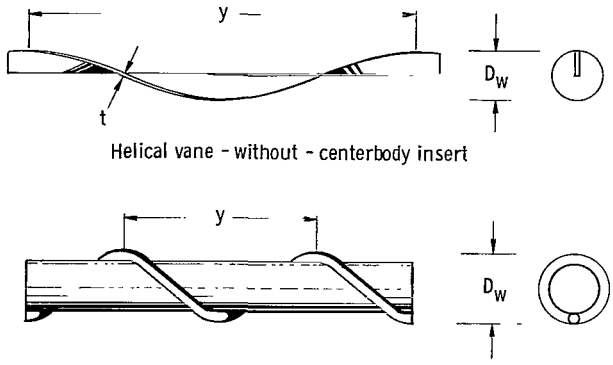

Figure 14. - Insert geometries similar to helical-vane insert.

expressions. A discussion of these experiments and the results obtained is presented in this section.

Pressure-loss and heat-transfer tests were conducted with a $Y/D_w = 1.75$ helical vane-without-centerbody insert. The vane of this insert extended from the tube wall to the tube axis. The tests were conducted with the same equipment and procedures previously described.

Pressure-loss tests were conducted with two different wire-wrapped plugs ($Y/D_w \cong 2.9$ and 2.7). The centerbody-diameter to tube-diameter ratios D_{cb}/D_w of these plugs were about 0.60 and 0.86, respectively. The pressure-loss tests of the plugs were conducted in a different apparatus. However, the flow circuitry and test equipment was similar to the apparatus previously described with the exception that heat addition was not possible. Thus, the pressure loss tests of the wire-wrapped plugs were conducted under adiabatic conditions. The tube into which the plugs were placed was a smooth, plastic pipe having an inner diameter of 2.22±0.01 centimeter. The test fluid was air. The plug inserts extended approximately 60 centimeters upstream of the inlet pressure tap providing a flow development length. Table IV presents the physical dimensions of the helical vane-without-centerbody and the wire-wrapped plugs as well as the standard deviations calculated from these measured dimensions.

The measured overall static-pressure losses and the measured heat-transfer coefficients of the helical vane-without-centerbody insert were reduced in accordance with equations (7) to (11), (16), and (17) with the centerbody diameter D_{cb} equal to zero. Friction factors and Stanton-Prandtl moduli for this insert are shown in figure 15. In addition, the correlating expressions, equations (15) and (18), are plotted on the individual figures. The experimental friction factor and Stanton-Prandtl modulus data both exhibit a trend with respect to Reynolds number that is similar to that described previously for the f_h and J_h data of the helical-vane inserts (figs. 10 and 11). The maximum deviation of the friction factor data from the correlating expression is about

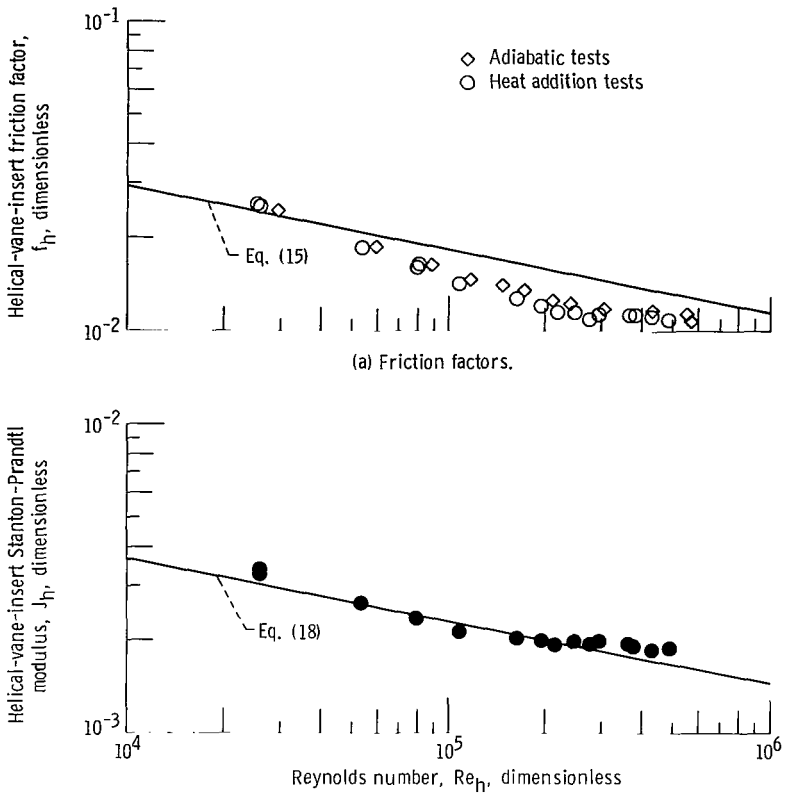

Figure 15. - Frictional pressure losses and heat transfer in tube with helical vane without centerbody insert. Insert pitch to tube diameter ratio, 1.75.

25 percent. The heat-transfer data for this insert configuration deviate a maximum of about 10 percent.

The pressure-loss data obtained with the wire-wrapped plugs were reduced in accordance with equations (7) to (11) modified, however, as follows. The wires were assumed rectangular in cross section rather than circular. The height of each rectangle was taken equal to the wire diameter and the width adjusted to yield equal cross-sectional area. The friction factors computed from the pressure-loss data are plotted in figure 16. Equation (15) is likewise plotted in this figure. For the $Y/D_W = 2.9$ wire-wrapped plug, the friction factors are all smaller in magnitude than predicted by equation (15), with the deviations increasing with increased Reynolds number. The maximum deviation of the data is about 30 percent.

The helical vane-without-centerbody and the wire-wrapped plugs may be considered as geometrical extremes of the helical-vane insert. As such, the data obtained from the experiments conducted with these inserts serve as a further test of the analysis pre-

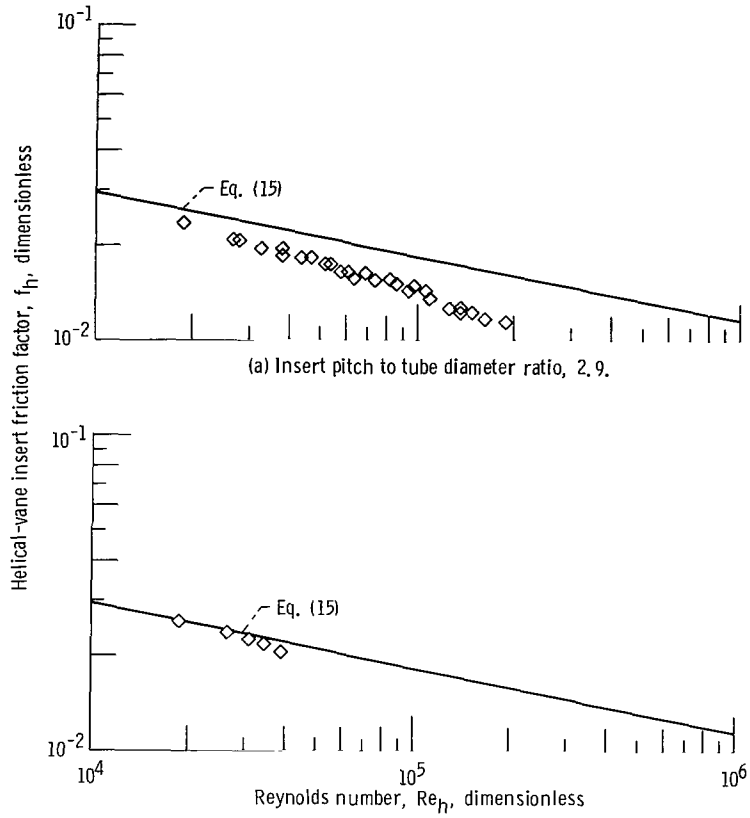

Figure 16. - Friction factors for wire-wrapped plugs.

sented in this report. The general agreement of the data with the correlations tends to support the applicability of the analysis to this class of insert.

APPLICATION TO TWISTED TAPES

The twisted tape is a swirl-generating insert that has been frequently studied and reported (ref. 9). Geometrically, it is equivalent to a double helical vane-without-centerbody insert. Consequently, twisted-tape experimental data may be expected to correlate as did the helical vane insert data. A discussion is presented in the following paragraphs of the comparison made of a limited amount of twisted-tape friction factor and heat-transfer data obtained from the literature with the expressions employed for the helical-vane insert.

Because of the geometrical similarity, the analysis of pressure losses in helical-vane inserts could be extended as shown in appendix D to the twisted tape. The results

of this extension were comparable to those described previously for the helical-vane insert. Therefore, the expressions for friction factor and heat transfer (eqs. (15) and (18), respectively), modified for the geometry of the twisted tape, would be expected to correlate experimental data. The authors of this report, however, did not conduct tests with the twisted-tape insert. Instead, the data of references 4 and 7 were employed for comparison.

References 4 and 7 present experimentally determined twisted-tape friction factors and corresponding Reynolds numbers. These friction factors and Reynolds numbers were defined by the cited references on the basis of an axial-flow model similar to that for the helical-vane insert. A composite plot of the data of these references is presented in figure 17. Equation (13) is likewise shown for comparison. Figure 17 indicates that twisted-tape (axial) friction factors increase substantially with decreasing Y/D_w.

The data of figure 17 were reduced to the friction factors f_t and Reynolds numbers Re_t as defined from the analysis of appendix D. (The equations employed to reduce these data are shown in appendix E.) The reduced data were then plotted as shown in figure 18. In addition, the following equation is shown as a curve in the same figure:

$$f_t = \frac{0.184}{Re_t^{0.2}} \tag{24}$$

The reduced friction factor data fall in a band above the line corresponding to equation (24). An average line drawn through the data would deviate from the correlating equation by approximately +20 percent for Reynolds number in excess of 10^4.

Reference 4 presents experimental Nusselt number and Reynolds number data for twisted tapes (as obtained by R. Koch[2]). These data were converted to axial Stanton-Prandtl moduli J_A as shown in appendix E. Figure 19 presents a plot of the converted J_A data of reference 4 as a function of axial Reynolds number. Equation (14), the correlation of heat transfer in a plain tube, is shown on this figure for comparison.

The data of figure 19 were reduced to Stanton-Prandtl moduli J_t and Reynolds numbers Re_t as defined by appendix D. These reduced data are plotted in figure 20 along with the correlating expression shown in the equation

$$J_t = 0.023(Re_t)^{-0.2} \tag{25}$$

[2]Koch, R.: Druckverlust und Warmeübergang bei verwirbelter Strömung. VDI - Forschungsheft, Series B, vol. 24, no. 469, 1958, pp. 1-41.

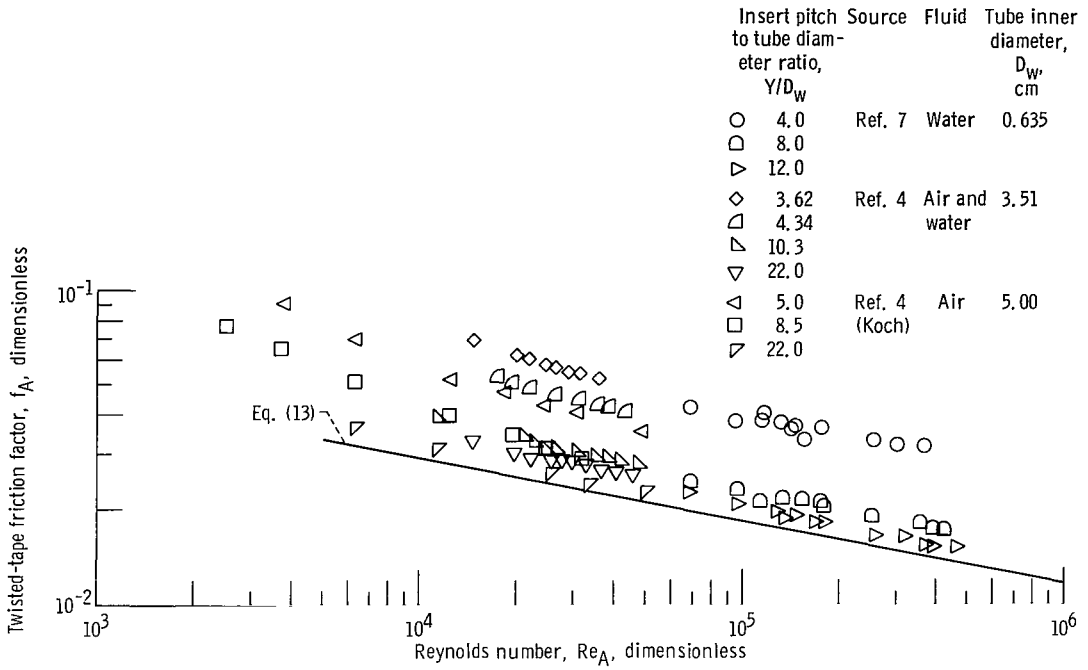

Figure 17. - Composite plot of twisted-tape friction factors obtained from references 4 and 7.

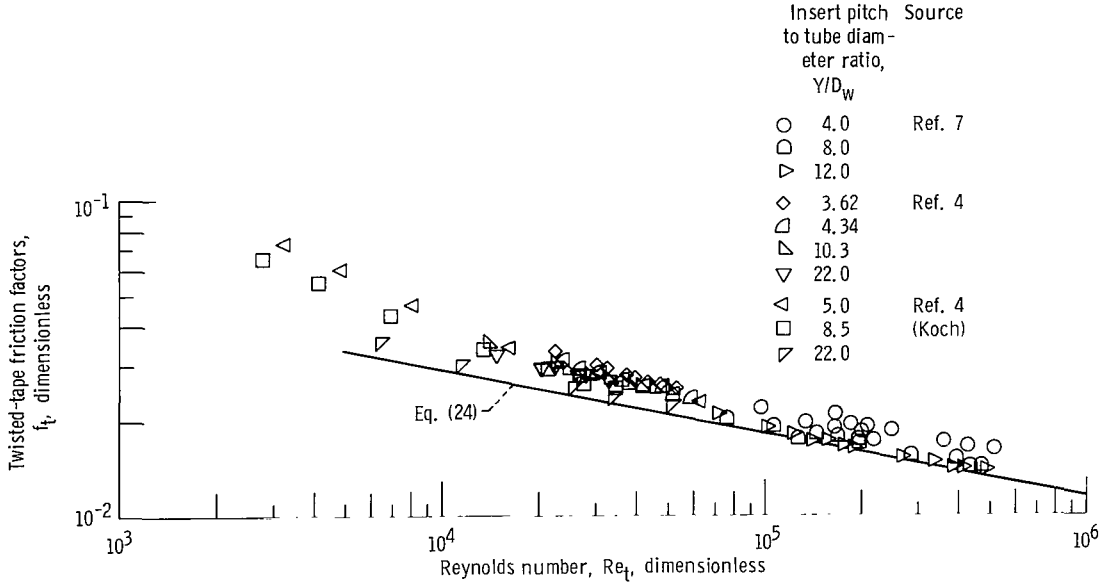

Figure 18. - Comparison of twisted-tape friction factors with correlating equation.

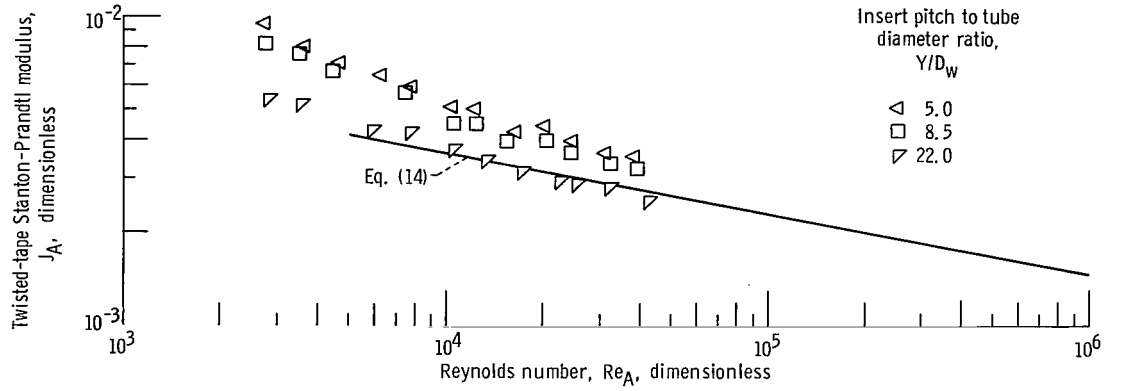

Figure 19. - Twisted-tape Stanton-Prandtl moduli obtained from reference 4. Fluid, air; tube inner diameter, 5.00 cm.

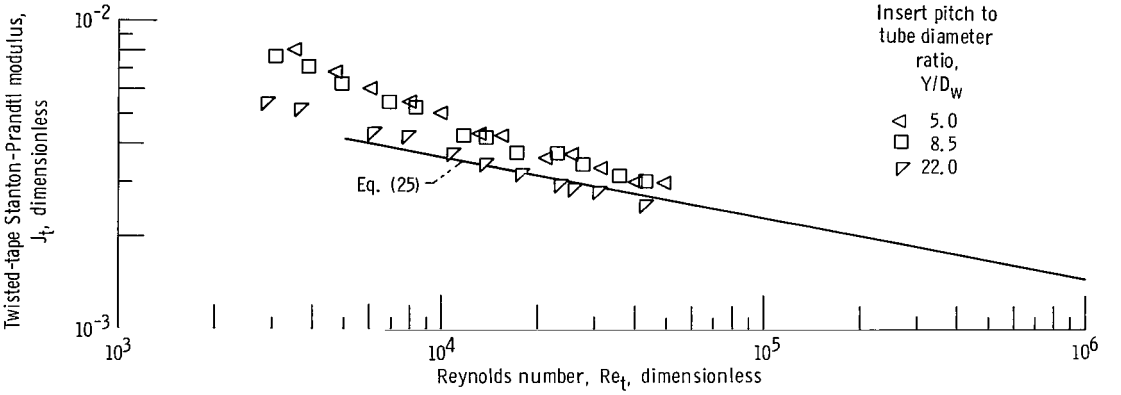

Figure 20. - Comparison of twisted-tape Stanton-Prandtl moduli from reference 4 with correlating equation.

Again, the data fall in a band which lies above the line corresponding to equation (25). An average line through the data would deviate by as much as +15 percent from a plot of equation (25) for Reynolds numbers above 10^4.

The following are possible explanations for the deviation of the twisted-tape friction factor and heat-transfer data from equations (24) and (25). The investigators may not have employed an adequate momentum pressure-loss correction to their measured overall pressure losses. The inserts may have made good thermal contact with the tube wall; consequently, the data of figure 19 may include a fin conduction effect not accounted for by equation (25). The investigators may have included flow and heat-transfer development regions in their experimental results; this would yield values of friction factors and heat-transfer coefficients in excess of the fully established values. Finally, secondary flow effects in twisted tapes may be more extensive than in helical-vane inserts. References 4 and 5 present experimental evidence for the existence of four secondary-

flow cells in tubes containing twisted tapes. Only two such flow cells are believed to occur in tubes containing helical-vane inserts. The additional secondary-flow patterns occurring with twisted tapes, believed due to the presence of two-flow passages, would also contribute to higher friction factors and heat-transfer coefficients than predicted. The resolution of the significance of each of these explanations awaits more definitive experiments. However, figures 18 and 20 suggest that the analysis of this report can reasonably predict the gross performance of twisted tapes.

SUMMARY OF RESULTS AND CONCLUSIONS

An analysis was conducted of flow inside a tube containing a helical-vane insert. This analysis assumed solid-body rotation of the flow and employed conservation of linear and angular momentum. The analysis resulted in a new equation for fully developed momentum pressure losses in tubes containing helical-vane inserts, an expression for the frictional pressure losses in tubes with these inserts, and a new theoretically based expression for the hydraulic diameter of tubes with helical inserts. Plain-tube expressions for friction factor and heat transfer, modified for the helical vane insert, were obtained from the analysis and were used to predict the performance of this insert.

A series of experiments was conducted to measure the pressure losses and local heat-transfer coefficients of air flowing inside a tube containing thermally passive helical-vane inserts. Four helical-vane inserts were tested having pitch to tube diameter ratios of 0.52, 0.75, 1.46, and 6.36. Tests were conducted over the range of Reynolds numbers from 30×10^3 to 300×10^3, with some data taken at Reynolds numbers beyond this range. Pressure-loss and heat-transfer coefficient data were also obtained from a limited series of experiments with two types of swirl-generating inserts representing geometrical extremes of the helical-vane insert. These inserts were a wire-wrapped plug and a helical vane having no centerbody. In general, the experimental data indicated that both the pressure losses and heat-transfer coefficients increased as the insert pitch to tube diameter ratio decreased.

Friction factors and Stanton-Prandtl moduli were computed from the experimental data of the four helical-vane inserts. These were compared with the corresponding modified plain-tube expressions obtained from the analysis. This comparison showed that, in the range of Reynolds numbers of 30×10^3 to 300×10^3, the friction factor and Stanton-Prandtl modulus data deviated from the predictions by about ±20 and ±15 percent, respectively, suggesting the analysis to be largely correct. The friction factor and Stanton-Prandtl modulus data for the wire-wrapped plugs and the helical vane-without-centerbody insert deviated from the appropriate modified plain-tube expressions

by a maximum of about 30 percent, tending to support the applicability of the analysis to this class of insert as well. Graphs were presented of normalized helical-vane-insert friction factors and Stanton-Prandtl moduli, plotted as a function of pitch to tube diameter ratio, which included data from the literature. The trends of these data were in good agreement with predictions. Based on these results, it was concluded that the pressure losses and heat-transfer coefficients for single-phase flow in tubes containing helical-vane inserts can reasonably be predicted from plain-tube expressions modified in accordance with the analysis presented herein.

The analysis of pressure losses in tubes containing helical vanes was extended to twisted-tape inserts. Comparable plain-tube expressions for friction factor and heat transfer, modified for the twisted-tape geometry, were obtained. A limited body of experimental twisted-tape friction factor and Stanton-Prandtl modulus data from the literature was compared with the expressions obtained from the analysis. The experimentally determined values of twisted-tape friction factor and Stanton-Prandtl modulus were somewhat larger in magnitude than the values predicted. However, the gross performance of the twisted-tape insert appeared to be predicted by the analysis.

The experimental friction factor and Stanton-Prandtl modulus data for the helical-vane inserts exhibited the following trend with Reynolds number. At low Reynolds numbers, the values of the aforementioned parameters decreased rapidly with increasing Reynolds numbers. At higher Reynolds numbers, these parameters tended to remain at a constant value or to increase slightly. This same characteristic was also observed with the experimental data for the wire plug and helical vane-without-centerbody inserts. The origin of this effect is so far unexplained.

Lewis Research Center,
National Aeronautics and Space Administration,
Cleveland, Ohio, July 24, 1970,
120-27.

APPENDIX A

SYMBOLS

A_c flow cross-sectional area perpendicular to axis of tube containing helical-vane insert, m^2

$A_{c,t}$ flow cross-sectional area perpendicular to axis of tube containing twisted-tape insert, m^2

C_p specific heat capacity, (W)(sec)/(kg)(K)

D diameter, m

D_e approximate equivalent diameter of tube containing twisted tape insert, m

D_h derived equivalent diameter of tube containing helical vane insert, m

D_t derived equivalent diameter of tube containing twisted tape insert, m

f friction factor

h local heat-transfer coefficient, $W/(m^2)(K)$

J Stanton-Prandtl modulus, dimensionless

k thermal conductivity, W/(m)(K)

l length, m

m mass flow rate, kg/sec

Nu Nusselt number, dimensionless

P pressure, N/m^2

P* static pressure at test section inlet pressure tap (see table III), N/m^2

Pr Prandtl number, dimensionless

p perimeter, m

Q test section net heat flux (see table III), W/m^2

r radius, m

Re Reynolds number, dimensionless

St Stanton number, dimensionless

T fluid bulk temperature or tube wall temperature (see table III), K

$\overline{T}$ arithmetic average fluid bulk temperature in test section or average tube wall temperature (see table III), K

t vane thickness, m

V local fluid velocity, m/sec

$\overline{V}$ fluid velocity based on test section average density, m/sec

V* maximum fluid velocity at test section outlet pressure tap (see table III), m/sec

Y insert pitch (axial distance for a 360^o revolution of the vane, tape or wire coil), m

α angle between tangent to vane and tube centerline (see fig. 2), rad

γ net pressure difference across vane of insert, N/m^2

ρ local density, kg/m^3

$\bar{\rho}$ density evaluated at arithmetic average of test section inlet and outlet temperatures and pressures, kg/m^3

τ shear stress, N/m^2

μ local viscosity, $(N)(sec)/m^2$

$\bar{\mu}$ viscosity evaluated at arithmetic average of test section inlet and outlet temperatures, $(N)(sec)/m^2$

Subscripts:

A reduced on the basis of axial flow model

cb centerbody

cs test section thermocouple center station

e exit

f frictional

h helical or helical vane insert

i inlet

m momentum

o plain tube

t twisted tape

v vane

w tube inner surface

z axial

θ tangential

APPENDIX B

ANALYSIS OF PRESSURE LOSSES IN TUBES CONTAINING HELICAL-VANE INSERTS

The analysis of pressure losses in tubes containing helical-vane inserts proceeds from the assumption that the fluid rotates at a constant angular speed and translates along the tube axis with a radially uniform constant velocity, that is, solid-body rotation with translation. The fluid streamlines are assumed to be parallel to the insert vane. Thus, the acute angle α between a tangent to a helical flow streamline and a line parallel to the tube axis is equal to the angle formed by a tangent to the vane at the same radial location (see fig. 2). The analysis developed on the basis of this assumption is, therefore, applicable to fully developed helical flow in which velocity profile distortions due to thick boundary layers or secondary flows may be neglected. A further assumption of the analysis is made: The radially uniform translation of each particle of flow is representable by the average axial velocity obtained from continuity; that is,

$$V_z = \frac{m}{A_c \rho} \tag{B1}$$

The secant and tangent of the angle α are related to the insert pitch and the radial displacement from the tube centerline as follows:

$$\sec \alpha = \frac{\left[Y^2 + (2\pi r)^2\right]^{1/2}}{Y} = \frac{l_h}{l_z} \tag{B2}$$

$$\tan \alpha = \frac{2\pi r}{Y} = \frac{l_\theta}{l_z} \tag{B3}$$

Pressures and shears at solid boundaries within the insert (shown in fig. 21) and the helical velocity may thus be resolved into axial and tangential components. Referring to

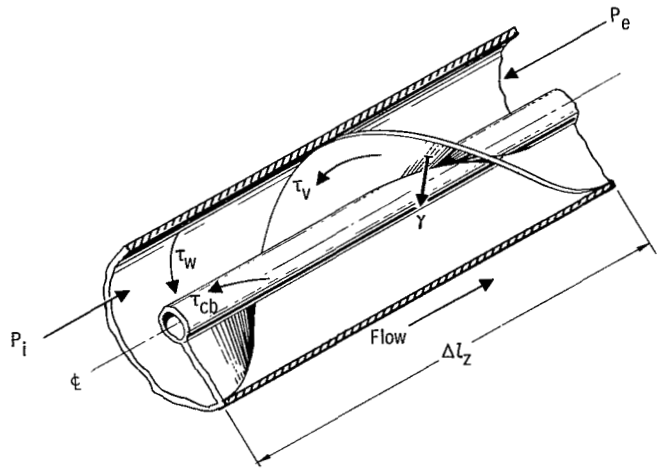

Figure 21. - Pressure and shear forces within helical-vane insert.

figure 21, application of momentum conservation in steady flow for an axial increment of length Δl_z yields the expression

$$\Delta P_z A_c - \tau_{h,w} \cos \alpha_w p_w \Delta l_z - \tau_{h,cb} \cos \alpha_{cb} p_{cb} \Delta l_z$$

$$- \left[\int_{r_{cb}}^{r_w} (2\tau_{h,v} \cos \alpha + \gamma \sin \alpha) \frac{dl_h}{dl_z} dr \right] \Delta l_z = m(V_{z,e} - V_{z,i}) \tag{B4}$$

The terms $p_w \Delta l_z$ and $p_{cb} \Delta l_z$ are the wetted surface areas of the tube and centerbody, respectively, within the increment Δl_z. The relations for these terms are given by

$$p_w \Delta l_z = \left(2\pi r_w - t \frac{dl_{h,w}}{dl_z} \right) \Delta l_z \tag{B5}$$

and

$$p_{cb} \Delta l_z = \left(2\pi r_{cb} - t \frac{dl_{h,cb}}{dl_z} \right) \Delta l_z \tag{B6}$$

The flow cross-sectional area normal to the tube axis is given by

$$A_c = \pi\left(r_w^2 - r_{cb}^2\right) - \int_{r_{cb}}^{r_w} t \sec \alpha \, dr \tag{B7}$$

Application of angular momentum conservation to the fluid within the same increment of length yields

$$\begin{aligned} &- r_w \tau_{h,w} \sin \alpha_w p_w \Delta l_z - r_{cb} \tau_{h,cb} \sin \alpha_{cb} p_{cb} \Delta l_z \\ &\quad - \left[\int_{r_{cb}}^{r_w} (2r\tau_{h,v} \sin \alpha - r\gamma \cos \alpha) \frac{dl_h}{dl_z} \, dr\right] \Delta l_z \\ &\quad = \left[\int_{r_{cb}}^{r_w} rV_\theta(\rho V_z) 2\pi r \, dr\right]_e - \left[\int_{r_{cb}}^{r_w} rV_\theta(\rho V_z) 2\pi r \, dr\right]_i \end{aligned} \tag{B8}$$

Substituting into equation (B8) the relations $(dl_h/dl_z) = \sec \alpha$ and $V_\theta = (V_z \tan \alpha)$ and multiplying by $2\pi/Y$ results in the following expression, after rearrangement:

$$\begin{aligned} \left(\int_{r_{cb}}^{r_w} \frac{2\pi r}{Y} \gamma \, dr\right) \Delta l_z &= \frac{2\pi^3}{Y^2}\left(r_w^4 - r_{cb}^4\right) \frac{m}{A_c} (V_{z,e} - V_{z,i}) \\ &\quad + \left(\int_{r_{cb}}^{r_w} 2\tau_{h,v} \tan^2 \alpha \, dr\right) \Delta l_z + \tau_{h,w} \tan \alpha_w \sin \alpha_w p_w \Delta l_z \\ &\quad + \tau_{h,cb} \tan \alpha_{cb} \sin \alpha_{cb} p_{cb} \Delta l_z \end{aligned} \tag{B9}$$

Substituting equation (B9) into equation (B4), collecting terms, and simplifying yield

$$\Delta P_z = \frac{m^2}{A_c^2}\left(\frac{1}{\rho_e} - \frac{1}{\rho_i}\right)\left[1 + \frac{2\pi^3}{Y^2}\frac{\left(r_w^4 - r_{cb}^4\right)}{A_c}\right] + \frac{\tau_{h,w} p_w}{A_c} \sec \alpha_w \Delta l_z$$

$$+ \frac{\tau_{h,cb} p_{cb}}{A_c} \sec \alpha_{cb} \Delta l_z + \frac{2}{A_c}\left(\int_{r_{cb}}^{r_w} \tau_{h,v} \sec^2 \alpha \, dr\right) \Delta l_z \qquad \text{(B10)}$$

The overall pressure loss across the increment Δl_z may be considered as the sum of momentum and frictional components as follows:

$$\Delta P_z = \Delta P_{m,h} + \Delta P_{f,h} \qquad \text{(B11)}$$

By inspection of equation (B10), the momentum pressure difference and the frictional pressure difference for the helical-vane insert can be written as

$$\Delta P_{m,h} = \frac{m^2}{A_c^2}\left(\frac{1}{\rho_e} - \frac{1}{\rho_i}\right)\left[1 + \frac{2\pi^3}{Y^2}\frac{\left(r_w^4 - r_{cb}^4\right)}{A_c}\right] \qquad \text{(B12)}$$

$$\Delta P_{f,h} = \left(\tau_{h,w}\frac{p_w}{A_c} \sec \alpha_w + \tau_{h,cb}\frac{p_{cb}}{A_c} \sec \alpha_{cb} + \frac{2}{A_c}\int_{r_{cb}}^{r_w} \tau_{h,v} \sec^2 \alpha \, dr\right) \Delta l_z \qquad \text{(B13)}$$

Equation (B12) may be divided by the momentum pressure difference for a plain tube. The resultant expression is based on equal mass-flow rates and identical inlet and outlet densities:

$$\frac{\Delta P_{m,h}}{\Delta P_{m,o}} = \left(\frac{A_{c,o}}{A_c}\right)^2\left[1 + \frac{2\pi^3}{Y^2}\frac{\left(r_w^4 - r_{cb}^4\right)}{A_c}\right] \qquad \text{(B14)}$$

A plot of the ratio $P_{m,h}/P_{m,o}$ as a function of the pitch to tube diameter ratio, that is, $Y/2r_w$, is shown in figure 22 for a tube inner diameter of 2.21 centimeters and center-

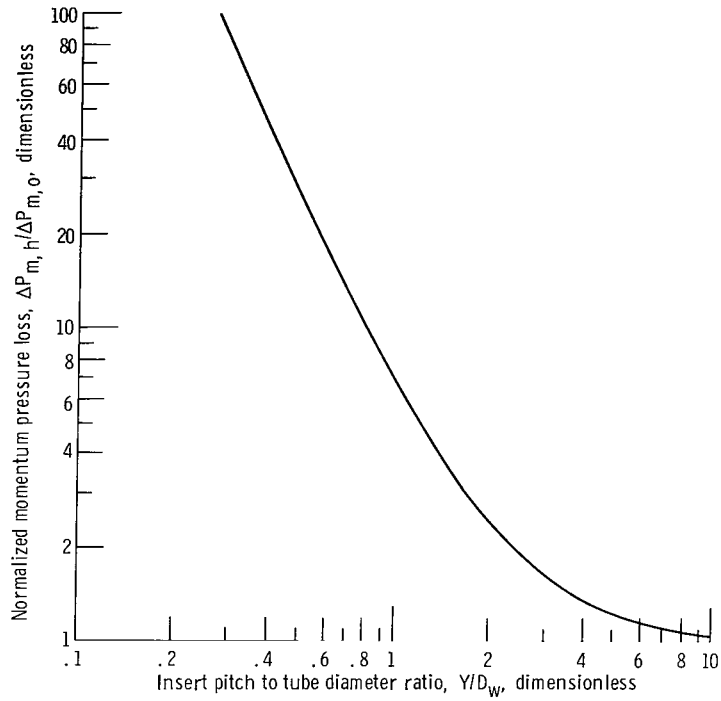

Figure 22. - Helical-vane-insert momentum pressure loss normalized to plain-tube momentum pressure loss. Ratio of centerbody diameter to tube inner diameter, 0.286; ratio of vane thickness to tube inner diameter, 0.068.

body diameter of 0.635 centimeter. From this figure it is clear that significant errors in the momentum pressure loss would occur if such were computed on the basis of a plain tube.

The shear stresses are defined as

$$\tau_{h,w} = \frac{f_w}{4}\rho\left(\frac{V_{h,w}^2}{2}\right)$$

$$\tau_{h,cb} = \frac{f_{cb}}{4}\rho\left(\frac{V_{h,cb}^2}{2}\right)$$

$$\tau_{h,v} = \frac{f_v}{4}\rho\left(\frac{V_{h,v}^2}{2}\right) \tag{B15}$$

The relation between the helical velocity V_h and the axial velocity V_z is given by

$$V_h = (V_z \sec \alpha) = \left(V_z \frac{l_h}{l_z}\right) \tag{B16}$$

Substituting equation (B15) into equation (B13) and using equation (B16) result in

$$\frac{\Delta P_{f,h}}{\Delta l_z} = \frac{f_w}{4} \sec^3 \alpha_w \left(\frac{\rho V_z^2}{2}\right) \frac{p_w}{A_c} + \frac{f_{cb}}{4} \sec^3 \alpha_{cb} \left(\frac{\rho V_z^2}{2}\right) \frac{p_{cb}}{A_c} + \frac{2}{A_c} \left[\int_{r_{cb}}^{r_w} \frac{f_v}{4} \sec^4 \alpha \left(\frac{\rho V_z^2}{2}\right) dr\right] \tag{B17}$$

The equality of the friction factors is now assumed:

$$f_w = f_{cb} = f_v \equiv f_h \tag{B18}$$

Substituting the helical friction factor into equation (B17) and collecting terms yields

$$\frac{\Delta P_{f,h}}{\Delta l_z} = \frac{f_h}{4A_c} \left(\frac{\rho V_z^2}{2}\right) \left(\sec^3 \alpha_w p_w + \sec^3 \alpha_{cb} p_{cb} + 2 \int_{r_{cb}}^{r_w} \sec^4 \alpha \, dr\right) \tag{B19}$$

The equivalent hydraulic diameter for the tube with the helical-vane insert is shown as

$$D_h = \frac{4A_c}{\left[p_w + \left(\frac{\sec^3 \alpha_{cb}}{\sec^3 \alpha_w}\right) p_{cb} + \left(\frac{2}{\sec^3 \alpha_w}\right) \int_{r_{cb}}^{r_w} \sec^4 \alpha \, dr\right]} \tag{B20}$$

Consequently, the frictional pressure loss for flow in a tube containing a helical-vane insert takes the simple form

$$\Delta P_{f,h} = \frac{f_h}{D_h} \sec^3 \alpha_w \left(\rho \frac{V_z^2}{2} \right) \Delta l_z$$

or

$$\frac{\Delta P_{f,h}}{\Delta l_z} = \frac{f_h}{D_h} \left(\frac{l_{h,w}}{l_z} \right)^3 \rho \frac{V_z^2}{2} \qquad \text{(B21)}$$

APPENDIX C

MODIFICATION OF CORRELATIONS TO PREDICT FRICTION FACTORS AND STANTON-PRANDTL MODULI ON AXIAL BASIS

The definition of the axial friction factor is given by

$$f_A = \frac{\Delta P_{f,h}}{\frac{l_z}{D_w} \rho \frac{V_z^2}{2}} \tag{C1}$$

The frictional pressure loss is

$$\Delta P_{f,h} = f_h \frac{l_{h,w}}{D_h} \rho \frac{V_{h,w}^2}{2} \tag{C2}$$

Substitution of (C2) into (C1) and normalizing to the plain-tube friction factor on the basis of equal axial velocities, fluid properties, and tube inner diameter yield

$$\frac{f_A}{f_o} = \frac{f_h}{f_o} \left(\frac{l_{h,w}}{l_z} \right)^3 \left(\frac{D_w}{D_h} \right) \tag{C3}$$

Equations (15) and (13) are employed to obtain f_h/f_o. The result is shown in equation (C4).

$$\frac{f_h}{f_o} = \left(\frac{D_w}{D_h} \right)^{0.2} \left(\frac{l_z}{l_{h,w}} \right)^{0.2} \tag{C4}$$

Substitution into (C3) yields

$$\frac{f_A}{f_o} = \left(\frac{D_w}{D_h} \right)^{1.2} \left(\frac{l_{h,w}}{l_z} \right)^{2.8} \tag{C5}$$

The Stanton-Prandtl modulus, based on the axial-flow model, is

$$J_A = \left(\frac{h}{C_p \rho V_z}\right)\left(\frac{C_p \mu}{k}\right)^{0.6} \tag{C6}$$

The heat-transfer coefficient h is given as

$$h = \frac{J_h \rho C_p V_{h,w}}{\left(\frac{C_p \mu}{k}\right)^{0.6}} \tag{C7}$$

Substitution of equation (C7) into (C6) and normalizing to J_o on the same basis stated previously yield

$$\frac{J_A}{J_o} = \frac{J_h}{J_o}\left(\frac{l_{h,w}}{l_z}\right) \tag{C8}$$

Equations (18) and (14) are used to obtain the ratio J_h/J_o. The result is shown as

$$\frac{J_h}{J_o} = \left(\frac{D_w}{D_h}\right)^{0.2}\left(\frac{l_z}{l_{h,w}}\right)^{0.2} \tag{C9}$$

Substitution of equation (C9) into (C8) yields

$$\frac{J_A}{J_o} = \left(\frac{D_w}{D_h}\right)^{0.2}\left(\frac{l_{h,w}}{l_z}\right)^{0.8} \tag{C10}$$

APPENDIX D

PRESSURE LOSSES IN TUBES CONTAINING TWISTED TAPES

The twisted tape may be considered geometrically as a helical insert having no centerbody, the vane of which extends diametrically across the tube. Equations (B4) and (B8) may be modified for the twisted tape such that

$$\Delta P_z A_{c,t} - \tau_{h,w} \cos \alpha_w p_w \Delta l_z - \left[\int_0^{r_w} 2(2\tau_{h,t} \cos \alpha + \gamma \sin \alpha) \frac{dl_h}{dl_z} dr \right] \Delta l_z = m(V_{z,e} - V_{z,i}) \tag{D1}$$

$$- r_w \tau_{h,w} \sin \alpha_w p_w \Delta l_z - \left[\int_0^{r_w} 2(2r\tau_{h,t} \sin \alpha - r\gamma \cos \alpha) \frac{dl_h}{dl_z} dr \right] \Delta l_z = \left[\int_0^{r_w} rV_\theta(\rho V_z) 2\pi r \, dr \right]_e - \left[\int_0^{r_w} rV_\theta(\rho V_z) 2\pi r \, dr \right]_i \tag{D2}$$

The definitions of the wetted area of the tube $p_w \Delta l_z$ and the flow cross-sectional area $A_{c,t}$ are for the tape

$$p_w \Delta l_z = \left(2\pi r_w - 2t \frac{dl_{h,w}}{dl_z} \right) \Delta l_z \tag{D3}$$

and

$$A_{c,t} = \pi r_w^2 - 2 \int_0^{r_w} t \sec \alpha \, dr \tag{D4}$$

Following the steps detailed in appendix B, the expression for the momentum pressure loss and the friction pressure loss for a tube containing a twisted tape is

$$\Delta P_{m,t} = \frac{m^2}{A_{c,t}^2}\left(\frac{1}{\rho_e} - \frac{1}{\rho_i}\right)\left(1 + \frac{2\pi^3 r_w^4}{Y^2 A_{c,t}}\right) \tag{D5}$$

$$\Delta P_{f,t} = \frac{f_t}{D_t}\sec^3\alpha_w\left(\rho\frac{V_z^2}{2}\right)\Delta l_z = \frac{f_t}{D_t}\left(\frac{l_{h,w}}{l_z}\right)^3 \rho\frac{V_z^2}{2}\Delta l_z \tag{D6}$$

where the twisted-tape equivalent hydraulic diameter is

$$D_t = \frac{4A_{c,t}}{p_w + \frac{4}{\sec^3\alpha_w}\int_0^{r_w}\sec^4\alpha\, dr} \tag{D7}$$

The Reynolds number for use with twisted-tape friction factors is given as

$$Re_t = \frac{D_t\overline{V}_z\left(\frac{l_{h,w}}{l_z}\right)\overline{\rho}}{\overline{\mu}} \tag{D8}$$

The Stanton-Prandtl modulus is defined as

$$J_t = \left(\frac{h_t}{C_p\rho V_z\frac{l_{h,w}}{l_z}}\right)(Pr)^{0.6} \tag{D9}$$

For use with J_t, the following local Reynolds number is defined:

$$Re_t = \frac{D_t V_z\left(\frac{l_{h,w}}{l_z}\right)\rho}{\mu} \tag{D10}$$

APPENDIX E

REDUCTION OF TWISTED-TAPE DATA

Friction Factor

References 4 and 7 define the axial friction factor and Reynolds number for a tube containing a twisted tape as follows:

$$f_A = \frac{\Delta P_{f,t}}{\left(\frac{l_z}{D_e}\right)\rho\frac{V_z^2}{2}} \tag{E1}$$

and

$$Re_A = \frac{D_e V_z \rho}{\mu} \tag{E2}$$

where the equivalent hydraulic diameter is

$$D_e = \frac{\pi D_w^2 - 4tD_w}{\pi D_w + 2(D_w - t)} \tag{E3}$$

The axial friction factors and Reynolds numbers were reduced to corresponding friction factors and Reynolds numbers defined by equations (D6) and (D8) as follows:

$$f_t = f_A\left(\frac{D_t}{D_e}\right)\left(\frac{l_z}{l_{h,w}}\right)^3 \tag{E4}$$

$$Re_t = Re_A\left(\frac{l_{h,w}}{l_z}\right)\left(\frac{D_t}{D_e}\right) \tag{E5}$$

Reference 4 presents twisted-tape Nusselt numbers as a function of axial Reynolds numbers. The Nusselt numbers were defined by this reference as

$$Nu_A = \frac{h_t D_w}{k} \tag{E6}$$

The Nusselt number data were converted to axial Stanton-Prandtl moduli by

$$J_A = \left(\frac{h_t}{C_p \rho V_z}\right)\left(\frac{C_p \mu}{k}\right)^{0.6} \tag{E7}$$

$$J_A = \left(\frac{Nu_A}{Re_A}\right)\left(\frac{D_e}{D_w}\right)\left(\frac{1}{Pr^{0.4}}\right) \tag{E8}$$

Reference 4 cites the value of 1.667 for D_w/D_e and 0.7 for the Prandtl number as applicable to the data.

The values of J_A and Re_A for the twisted-tape data of reference 4 were reduced to corresponding values of the Stanton-Prandtl modulus and Reynolds number given by equations (D9) and (D10). The axial Reynolds number was reduced in accordance with equation (E5), and the following equation was used to obtain values of J_t:

$$J_t = J_A\left(\frac{l_z}{l_{h,w}}\right) \tag{E9}$$

REFERENCES

1. Peterson, J. R.: High-Performance "Once-Through" Boiling of Potassium in Single Tubes at Saturation Temperatures of 1500° to 1750° F. NASA CR-842, 1967.

2. Bond, J. A.; and Converse, G. L.: Vaporization of High-Temperature Potassium in Forced Convection at Saturation Temperatures of 1800° to 2100° F. NASA CR-843, 1967.

3. Peterson, J. R.; Weltmann, R. N.; and Gutstein, M. U.: Thermal Design Procedures for Space Rankine Cycle System Boilers. Intersociety Energy Conversion Engineering Conference. Vol. 1. IEEE, 1968, pp. 313-328.

4. Smithberg, E.; and Landis, F.: Friction and Forced Convection Heat-Transfer Characteristics in Tubes with Twisted Tape Swirl Generators. J. Heat Transfer, vol. 86, no. 1, Feb. 1964, pp. 39-49.

5. Seymour, Errol V.: Fluid Flow Through Tubes Containing Twisted Tapes. The Engineer, vol. 222, Oct. 28, 1966, pp. 634-642.

6. Gambill, W. R.; Bundy, R. D.; and Wansbrough, R. W.: Heat Transfer, Burnout, and Pressure Drop for Water in Swirl Flow Through Tubes with Internal Twisted Tapes. Rep. ORNL-2911, Oak Ridge National Lab., Apr. 1960.

7. Feinstein, Lester; and Lundberg, R. E.: Fluid Friction and Boiling Heat Transfer with Water in Vortex Flow in Tubes Containing an Internal Twisted Tape. Stanford Research Inst. (RADC-TDR-63-451, DDC No. AD-430889), June 1963.

8. Poppendiek, H. F.; and Gambill, W. R.: Helical, Forced-Flow Heat Transfer and Fluid Dynamics in Single and Two-Phase Systems. Reactor Engineering and Equipment. Vol. 8 of Proceedings of the Third International Conference on the Peaceful Uses of Atomic Energy. United Nations, 1965, pp. 274-285.

9. Bergles, Arthur E.; and Morton, Harmon L.: Survey and Evaluation of Techniques to Augment Convective Heat Transfer. Rep. TR-5382-34, Dept. Mech. Eng., Massachusetts Inst. Tech., Feb. 1965. (Available from DDC as AD-619511.)

10. Sams, E.: Heat Transfer and Pressure-Drop Characteristics of Wire-Coil Type Turbulence Promotors. Presented at USAEC Reactor Heat Transfer Conference, New York, N. Y., Nov. 1956.

11. Goldner, C.: Forming a Helicoid. Design News, May 26, 1965.

12. Poppendiek, H. F.; Greene, N. D.; Sabin, C. M.; Fergenbutz, L. V.; and Mouritzen, G.: High Acceleration Field Heat Transfer for Auxiliary Space Nuclear Power Systems. Rep. GLR-42, Geosciences, Ltd. (AEC Rep. SAN-409-29), Jan. 1966.

13. Anon.: Fluid Meters; Their Theory and Applications. ASME.

14. Dean, Robert C., Jr.: Aerodynamic Measurements. Massachusetts Inst. Tech., Gas Turbine Lab., 1953.

15. Beers, Yardley: Introduction to the Theory of Error. Second ed., Addison-Wesley Publ. Co., 1957.

16. McAdams, William H.: Heat Transmission. Third ed., McGraw-Hill Book Co., Inc., 1954.

17. Schlichting, Hermann (J. Kestin, trans.): Boundary Layer Theory. Fourth ed., McGraw-Hill Book Co., Inc., 1960.

18. Gutstein, Martin U.; Converse, George L.; and Peterson, Jerry R.: Augmentation of Single-Phase Heat Transfer in Tubes by Use of Helical Vane Inserts. Presented at the Fourth International Heat Transfer Conference, Versailles/Paris, France, Aug. 31-Sept. 5, 1970.

TABLE I. - PHYSICAL DIMENSIONS OF HELICAL VANE INSERTS

Insert pitch to tube diameter ratio, Y/D_w	Insert equivalent diameter, D_h, cm	Ratio of equivalent diameter to conventional hydraulic diameter, D_h/D_e, dimensionless	Pitch		Centerbody diameter		Vane thickness	
			Average, cm	Standard deviation, percent	Average, cm	Standard deviation, percent	Average, cm	Standard deviation, percent
0.52	1.37	1.03	1.166	0.9	0.648	2.1	0.086	1.1
.75	1.51	1.11	1.623	.9	.592	1.5	.140	1.6
1.46	1.63	1.22	3.261	1.4	.630	.4	.193	1.5
6.36	1.43	1.08	14.044	13.1	.635	0	.185	.4

TABLE II. - ESTIMATED COMBINED PROBABLE ERRORS IN HELICAL PARAMETERS

Insert pitch to tube diameter ratio, Y/D_w	Probable errors, percent		
	Helical friction factors, f_h	Helical Reynolds numbers, Re_h	Helical Stanton parameters, St_h
0.52	6.8	2.9	2.9
.75	6.8	2.9	2.9
1.46	7.6	3.1	3.1
6.36	11.9	5.0	4.6

TABLE III. - EXPERIMENTAL AND COMPUTED DATA

(a) Helical-vane-insert pitch to tube diameter ratio, 0.52

(a-1) Pressure-loss and heat-transfer data.

Air mass flow rate, m, kg/sec	Air inlet bulk temperature, T_1, K	Air average bulk temperature, $\bar{T}$, K	Static pressure at inlet tap, P^*, N/m^2	Overall static pressure loss, $\Delta P_{z,2}$, N/m^2	Maximum helical velocity at outlet tap, $V_{h,w}$, m/sec	Frictional pressure loss, $\Delta P_{f,h}$, N/m^2	Friction factor, f_h, dimensionless	Reynolds number for friction, Re_h, dimensionless	Air bulk temperature at center station, T_{cs}, K	Net heat flux, Q, w/m^2	Inner wall average temperature at center station, $\bar{T}_{w,cs}$, K	Heat-transfer coefficient at center station, h_{cs}, $w/(m^2)(K)$	Reynolds number at center station, $Re_{h,cs}$, dimensionless	Stanton-Prandtl number at center station, $J_{h,cs}$, dimensionless
2.04×10^{-2}	296.6	359.3	4.462×10^5	1.982×10^5	2.00×10^2	1.662×10^5	1.34×10^{-2}	2.66×10^5	359.4	3.63×10^4	401.1	8.74×10^2	2.66×10^5	1.69×10^{-3}
1.73	296.0	369.2	3.986	1.711	2.02	1.430	1.36	2.21	369.5	3.60	416.8	7.63	2.21	1.73
1.33	297.5	383.2	3.154	1.306	1.94	1.099	1.41	1.65	383.5	3.22	436.1	6.14	1.65	1.81
1.09	295.2	387.9	2.725	1.062	1.82	9.023×10^4	1.48	1.35	388.2	2.87	440.1	5.54	1.35	1.98
9.50×10^{-3}	296.7	396.6	2.471	9.165×10^4	1.75	7.834	1.53	1.16	396.9	2.69	450.3	5.05	1.16	2.07
7.74	297.3	407.2	2.150	7.305	1.63	6.302	1.60	9.25×10^4	407.5	2.41	462.2	4.42	9.24×10^4	2.22
5.35	296.3	414.4	2.016	4.698	1.06	4.280	2.28	6.32	414.7	1.79	464.4	3.60	6.31	2.62
3.45	296.3	437.2	1.419	2.871	1.02	2.605	2.21	3.93	473.7	1.38	486.4	2.83	3.92	3.17
5.06	295.6	415.6	1.657	4.363	1.28	3.868	1.81	5.97	416.0	1.72	468.8	3.26	5.96	2.50
4.30	296.5	423.4	1.533	3.593	1.16	3.216	1.93	5.00	423.8	1.54	478.0	2.85	4.99	2.57
3.32	297.8	446.2	1.389	2.697	1.01	2.442	2.16	3.73	446.7	1.39	501.6	2.54	3.72	2.95
2.73	298.3	463.3	1.307	2.181	8.52×10^1	2.009	2.42	2.99	463.8	1.27	518.2	2.34	2.98	3.29
2.45	298.8	467.8	1.266	1.904	7.74	1.766	2.56	2.66	468.4	1.17	524.4	2.09	2.66	3.27
2.09	299.7	470.6	1.212	1.542	6.72	1.442	2.76	2.27	471.1	1.01	522.9	1.95	2.26	3.57
1.73	299.8	471.2	1.159	1.194	5.67	1.125	3.03	1.88	471.7	8.41×10^3	520.7	1.72	1.88	3.78
1.21	300.0	482.1	1.095	7.244×10^3	4.02	6.915×10^3	3.60	1.29	482.6	6.23	527.9	1.38	1.29	4.34

(a-2) Adiabatic pressure-loss data.

Air mass flow rate, m, kg sec	Air inlet bulk temperature, T_1, K	Air average bulk temperature, $\bar{T}$, K	Static pressure at inlet tap, P^*, N/m^2	Overall static pressure loss, ΔP_z, N/m^2	Maximum helical velocity at outlet tap, $V_{h,w}$, m/sec	Frictional pressure loss, $\Delta P_{f,h}$, N/m^2	Friction factor, f_h, dimensionless	Reynolds number for friction, Re_h, dimensionless
2.46×10^{-3}	295.0	295.0	1.124×10^5	1.048×10^4	4.10×10^1	1.036×10^4	2.15×10^{-2}	3.73×10^4
4.34	295.4	295.4	1.295	2.513	7.08	2.436	1.77	6.56
6.20	296.1	296.1	1.538	4.539	9.76	4.309	1.72	9.36
8.05	296.8	296.8	1.789	6.578	1.22×10^2	6.116	1.61	1.21×10^5
1.09×10^{-2}	297.6	297.5	2.219	9.892	1.52	8.947	1.52	1.64
1.26	297.9	297.8	2.484	1.185×10^5	1.66	1.058×10^5	1.48	1.88
1.39	297.2	297.1	2.705	1.346	1.75	1.191	1.46	2.09
1.60	297.6	297.5	3.045	1.587	1.88	1.387	1.43	2.40
1.81	297.7	297.6	3.410	1.833	1.97	1.588	1.41	2.72
2.15	298.1	298.0	3.992	2.220	2.09	1.900	1.37	3.23
1.10	299.4	299.3	2.363	9.115×10^4	1.31	8.403×10^4	1.53	1.64
9.81×10^{-3}	299.8	299.8	2.170	7.931	1.23	7.365	1.57	1.47
8.53	299.5	299.4	1.967	6.656	1.13	6.237	1.62	1.28
6.98	299.8	299.7	1.729	5.107	9.90×10^1	4.844	1.69	1.04
4.93	299.3	299.3	1.429	3.145	7.63	3.039	1.84	7.38×10^4
4.45	298.7	298.7	1.365	2.699	6.99	2.620	1.89	6.66
3.86	298.5	298.5	1.293	2.188	6.18	2.136	1.97	5.78
3.19	298.5	298.5	1.217	1.650	5.22	1.621	2.10	4.78
2.24	298.4	298.4	1.124	9.875×10^3	3.75	9.781×10^3	2.44	3.35
1.57	298.4	298.5	1.071	5.889	2.67	5.860	2.87	2.35
6.36	294.2	294.2	1.610	4.251×10^4	9.10	4.005×10^4	1.65	9.64
5.75	294.5	294.4	1.524	3.703	8.46	3.551	1.69	8.72
5.08	294.4	294.4	1.432	3.095	7.67	2.986	1.74	7.70
4.30	294.5	294.5	1.339	2.432	6.65	2.365	1.83	6.51
3.84	294.4	294.4	1.285	2.053	6.03	2.005	1.90	5.81
3.31	294.4	294.4	1.228	1.661	5.29	1.630	2.00	5.02
2.75	294.2	294.2	1.171	1.245	4.46	1.228	2.11	4.18
1.96	294.1	294.1	1.105	7.508×10^3	3.22	7.453×10^3	2.45	2.97
1.53	294.0	294.0	1.072	5.194	2.54	5.169	2.72	2.32
8.86×10^{-4}	294.0	294.0	1.033	2.261	1.49	2.258	3.46	1.35

TABLE III - Continued. EXPERIMENTAL AND COMPUTED DATA

(b) Helical-vane-insert pitch to tube diameter ratio, 0.75

(b-1) Pressure-loss and heat-transfer data.

Air mass flow rate, m, kg/sec	Air inlet bulk temperature, T_i, K	Air average bulk temperature, $\bar{T}$, K	Static-pressure at inlet tap P^*, N/m^2	Overall static pressure loss, ΔP_z, N/m^2	Maximum helical velocity at outlet tap, $V_{h,w}$, m/sec	Frictional pressure loss, $\Delta P_{f,h}$, N/m^2	Friction factor, f_h, dimensionless	Reynolds number for friction, Re_h, dimensionless	Air bulk temperature at center station, T_{cs}, K	Net heat flux, Q, w/m^2	Inner wall average temperature at center station, $\bar{T}_{w,cs}$, K	Heat-transfer coefficient at center station, h_{cs}, $w/(m^2)(K)$	Reynolds number at center station, $Re_{h,cs}$, dimensionless	Stanton-Prandtl number at center station, $J_{h,cs}$, dimensionless
2.54×10^{-2}	303.1	346.8	2.892×10^5	1.162×10^5	2.22×10^2	9.077×10^4	1.13×10^{-2}	2.51×10^5	347.0	3.16×10^4	386.1	8.19×10^2	2.51×10^5	1.90×10^{-3}
2.53	303.9	348.5	2.892	1.174	2.24	9.150	1.14	2.50	348.6	3.21	387.8	8.32	2.50	1.93
3.08	298.6	335.2	3.420	1.459	2.26	1.143×10^5	1.16	3.13	335.4	3.22	367.6	1.01×10^3	3.13	1.94
2.57	301.5	344.8	2.954	1.221	2.23	9.571×10^4	1.18	2.56	344.9	3.18	383.1	8.43×10^2	2.56	1.92
2.53	303.7	347.9	2.890	1.180	2.25	9.207	1.14	2.50	348.1	3.19	388.3	8.02	2.50	1.86
2.38	304.4	351.7	2.775	1.114	2.21	8.716	1.16	2.34	351.8	3.21	393.7	7.77	2.34	1.91
2.12	304.3	356.8	2.548	9.875×10^4	2.16	7.774	1.19	2.06	356.9	3.17	402.6	7.01	2.06	1.93
1.79	304.9	366.1	2.263	8.286	2.07	6.570	1.24	1.71	366.4	3.12	417.8	6.11	1.71	1.99
1.54	304.3	376.4	2.046	7.001	1.98	5.578	1.28	1.44	376.7	3.15	433.8	5.54	1.43	2.10
1.31	304.3	389.2	1.877	5.946	1.88	4.784	1.36	1.20	389.5	3.15	454.6	4.87	1.19	2.16
1.05	303.3	409.8	1.671	4.684	1.74	3.796	1.46	9.24×10^4	410.1	3.16	485.0	4.24	9.22×10^4	2.34
4.11	303.1	329.8	4.374	1.907×10^5	2.30	1.493×10^5	1.10	4.23×10^5	329.9	3.14	354.4	1.31×10^3	4.23×10^5	1.88
5.06	304.5	326.3	5.287	2.347	2.32	1.839	1.09	5.25	326.4	3.16	346.0	1.66	5.24	1.94
5.84	303.1	321.6	6.213	2.787	2.25	2.223	1.17	6.12	321.7	3.11	337.6	2.03	6.11	2.05
7.60×10^{-3}	301.8	409.4	1.414	3.068×10^4	1.38	2.589×10^4	1.66	6.71×10^4	409.7	2.32	476.6	3.48×10^2	6.70×10^4	2.64
5.35	304.3	426.9	1.248	1.962	1.08	1.701	1.92	4.59	427.2	1.86	492.7	2.84	4.58	3.06
5.06	304.6	432.9	1.234	1.853	1.05	1.612	1.99	4.30	433.3	1.84	500.0	2.76	4.29	3.13

(b-2) Adiabatic pressure-loss data.

Air mass flow rate, m, kg/sec	Air inlet bulk temperature, T_i, K	Air average bulk temperature, $\bar{T}$, K	Static-pressure at inlet tap, P^*, N/m^2	Overall static pressure loss, ΔP_z, N/m^2	Maximum helical velocity at outlet tap, $V_{h,w}$, m/sec	Frictional pressure loss, $\Delta P_{f,h}$, N/m^2	Friction factor, f_h, dimensionless	Reynolds number for friction, Re_h, dimensionless
5.17×10^{-3}	296.4	296.4	1.152×10^5	1.188×10^4	5.75×10^1	1.162×10^4	1.92×10^{-2}	5.78×10^4
1.07×10^{-2}	299.5	299.4	1.507	3.588	1.08×10^2	3.356	1.55	1.19×10^5
1.53	299.2	299.1	1.892	5.831	1.36	5.293	1.45	1.70
1.55	300.1	300.0	1.892	5.966	1.39	5.394	1.43	1.71
2.61	301.6	301.4	2.341	8.604	1.63	7.568	1.35	2.27
2.58	302.2	302.0	2.811	1.125×10^5	1.79	9.696	1.30	2.83
2.61	297.5	297.3	2.826	1.143	1.79	9.839	1.31	2.91
2.61	299.2	299.0	2.802	1.177	1.86	1.006×10^5	1.31	2.89
3.14	300.2	300.0	3.235	1.404	1.99	1.176	1.21	3.47
4.13	300.1	299.8	4.175	1.884	2.10	1.555	1.18	4.58
4.63	301.4	301.1	4.662	2.121	2.12	1.745	1.17	5.10
4.98	301.1	300.8	5.000	2.293	2.14	1.882	1.18	5.49
5.57	304.1	303.8	5.592	2.577	2.17	2.108	1.15	6.10
5.51	305.5	305.2	5.714	2.631	2.11	2.181	1.24	6.01
6.12	305.2	304.9	6.302	2.922	2.14	2.412	1.23	6.68
4.07	304.3	304.0	4.144	1.864	2.10	1.540	1.18	4.45
1.54	302.5	302.4	1.821	5.800×10^4	1.45	5.202×10^4	1.34	1.69
6.02×10^{-3}	298.1	298.0	1.171	1.479	6.80×10^1	1.435	1.75	6.70×10^4
5.75	298.2	298.2	1.161	1.384	6.50	1.347	1.79	6.39
5.32	299.6	299.6	1.140	1.238	6.08	1.208	1.84	5.89
4.97	299.8	299.8	1.123	1.113	5.71	1.090	1.88	5.51
4.61	299.7	299.7	1.110	1.003	5.31	9.340×10^3	1.96	5.10
4.20	300.2	300.2	1.093	8.772×10^3	4.87	8.633	2.05	4.65
3.72	300.5	300.5	1.072	7.331	4.34	7.237	2.15	4.11
3.22	300.7	300.7	1.055	5.864	3.77	5.808	2.29	3.55
2.65	300.8	300.8	1.035	4.398	3.12	4.369	2.51	2.92
1.84	301.0	301.0	1.012	2.547	2.18	2.539	2.97	2.03
1.52	301.3	301.3	1.004	1.915	1.81	1.909	3.25	1.68

TABLE III. - Continued. EXPERIMENTAL AND COMPUTED DATA

(c) Helical-vane-insert pitch to tube diameter ratio, 1.46

(c-1) Pressure-loss and heat-transfer data.

Air mass flow rate, m, kg/sec	Air inlet bulk temperature, T_i, K	Air average bulk temperature, $\bar{T}$, K	Static-pressure at inlet tap P^*, N/m^2	Overall static pressure loss, ΔP_z, N/m^2	Maximum helical velocity at outlet tap, $V_{h,w}$, m/sec	Frictional pressure loss, $\Delta P_{f,h}$, N/m^2	Friction factor, f_h, dimensionless	Reynolds number for friction, Re_h, dimensionless	Air bulk temperature at center station, T_{cs}, K	Net heat flux, Q, w/m^2	Inner wall average temperature at center station, $\bar{T}_{w,cs}$, K	Heat-transfer coefficient at center station h_{cs}, $w/(m^2)(K)$	Reynolds number at center station, $Re_{h,cs}$, dimensionless	Stanton-Prandtl number at center station, $J_{h,cs}$, dimensionless
6.74×10^{-2}	291.4	310.5	3.268×10^{5}	1.059×10^{5}	2.05×10^{2}	7.999×10^{4}	1.31×10^{-2}	4.13×10^{5}	310.6	3.81×10^{4}	342.8	1.26×10^{3}	4.13×10^{5}	2.10×10^{-3}
6.07	298.5	320.3	3.004	9.791×10^{4}	2.10	7.350	1.32	3.64	320.5	3.90	356.5	1.14	3.63	2.11
5.31	298.0	322.8	2.660	8.726	2.11	6.523	1.35	3.16	322.9	3.86	361.6	1.05	3.16	2.21
4.38	299.5	329.4	2.298	7.280	2.05	5.482	1.41	2.57	329.6	3.82	374.3	8.90×10^{2}	2.57	2.27
3.05	299.4	342.9	1.796	4.887	1.84	3.749	1.54	1.74	343.1	3.82	399.7	6.92	1.74	2.53
5.24	294.6	319.2	2.562	8.379	2.14	6.171	1.27	3.15	319.4	3.79	359.7	9.87	3.15	2.11
5.08	294.1	319.6	2.523	8.125	2.09	6.033	1.30	3.05	319.8	3.80	360.9	9.66	3.05	2.13
4.50	294.0	323.9	2.297	7.209	2.06	5.358	1.34	2.67	324.0	3.92	370.8	8.71	2.67	2.17
3.84	296.0	330.5	2.044	6.113	2.00	4.565	1.37	2.25	330.6	3.85	381.4	7.86	2.25	2.28
2.91	296.0	338.0	1.722	4.388	1.76	3.386	1.50	1.68	338.2	3.52	395.4	6.31	1.68	2.41
1.82	300.7	347.6	1.350	2.325	1.32	1.911	1.72	1.03	347.8	2.44	404.5	4.37	1.03	2.66
2.48	300.7	343.7	1.525	3.517	1.67	2.743	1.48	1.41	343.9	3.06	402.5	5.34	1.41	2.40
2.51	298.4	341.2	1.550	3.548	1.65	2.776	1.50	1.44	341.4	3.09	399.3	5.44	1.43	2.42
2.27	300.1	339.5	1.466	3.044	1.52	2.447	1.55	1.30	339.6	2.56	391.6	5.04	1.30	2.47
2.00	299.7	341.4	1.388	2.581	1.39	2.109	1.63	1.15	341.5	2.39	394.3	4.61	1.15	2.56
1.68	301.9	348.4	1.297	2.039	1.24	1.693	1.74	9.46×10^{4}	348.6	2.23	404.7	4.02	9.45×10^{4}	2.66
1.33	303.6	356.7	1.218	1.488	1.05	1.261	1.92	7.39	356.8	2.01	416.3	3.41	7.38	2.84
1.09	304.7	362.1	1.159	1.127	8.99×10^{1}	9.693×10^{3}	2.08	5.99	362.3	1.78	421.6	3.03	5.98	3.07
7.78×10^{-3}	296.4	355.2	1.094	6.312×10^{3}	6.40	5.557	2.32	4.32	355.4	1.30	410.6	2.36	4.32	3.36

(c-2) Adiabatic pressure-loss data.

Air mass flow rate, m, kg/sec	Air inlet bulk temperature, T_i, K	Air average bulk temperature, $\bar{T}$, K	Static-pressure at inlet tap, P^*, N/m^2	Overall static pressure loss, ΔP_z, N/m^2	Maximum helical velocity at outlet tap, $V_{h,w}$, m/sec	Frictional pressure loss, $\Delta P_{f,h}$, N/m^2	Friction factor, f_h, dimensionless	Reynolds number for friction, Re_h, dimensionless
9.60×10^{-2}	289.2	288.5	4.377×10^{5}	1.417×10^{5}	1.91×10^{2}	1.144×10^{5}	1.33×10^{-2}	6.26×10^{5}
8.73	287.9	287.2	3.927	1.278	1.93	1.026	1.30	5.71
7.62	288.6	287.9	3.471	1.130	1.91	9.114×10^{4}	1.34	4.98
6.98	289.4	288.7	3.187	1.042	1.92	8.402	1.34	4.55
6.28	292.6	291.9	2.902	9.436×10^{4}	1.91	7.644	1.36	4.05
5.41	295.9	295.2	2.551	8.218	1.88	6.710	1.40	3.46
4.46	295.7	295.1	2.148	6.629	1.81	5.485	1.43	2.85
3.47	295.4	294.9	1.780	4.870	1.62	4.162	1.52	2.22
1.98	296.8	296.6	1.318	2.165	1.09	2.000	1.76	1.26
5.41	296.1	295.4	2.496	8.049	1.93	6.507	1.33	3.45
4.90	295.0	294.7	2.290	7.221	1.88	5.866	1.35	3.14
4.20	295.4	295.1	2.282	6.037	1.51	5.263	1.69	2.69
3.82	296.3	295.8	1.873	5.371	1.73	4.498	1.41	2.44
3.43	297.5	297.0	1.742	4.667	1.63	3.975	1.44	2.18
3.00	298.0	297.6	1.600	3.856	1.50	3.355	1.49	1.90
2.46	298.1	297.9	1.436	2.892	1.31	2.593	1.57	1.56
1.92	296.4	296.2	1.289	1.979	1.07	1.833	1.68	1.22
1.11	296.4	296.3	1.114	8.455×10^{3}	6.51×10^{1}	8.202×10^{3}	2.05	7.04×10^{4}
2.43	290.0	289.8	1.413	2.716×10^{4}	1.26×10^{2}	2.443×10^{4}	1.53	1.58×10^{5}
2.16	289.9	289.7	1.342	2.286	1.15	2.090	1.60	1.40
1.89	290.1	289.9	1.274	1.847	1.03	1.716	1.65	1.23
1.74	290.3	290.2	1.238	1.623	9.58×10^{1}	1.522	1.70	1.13
1.54	291.1	291.0	1.196	1.336	8.63	1.267	1.75	9.96×10^{4}
1.32	291.4	291.4	1.151	1.065	7.55	1.022	1.86	8.54
1.09	291.9	291.9	1.111	7.779×10^{3}	6.31	7.555×10^{3}	1.97	7.04
9.73×10^{-3}	291.9	291.9	1.092	6.511	5.66	6.358	2.05	6.28
8.54	293.4	293.4	1.072	5.318	5.03	5.219	2.15	5.49
7.03	292.5	292.5	1.050	3.852	4.16	3.802	2.29	4.53
4.96	293.6	293.6	1.027	2.212	2.97	2.197	2.60	3.18

TABLE III. - Concluded. EXPERIMENTAL AND COMPUTED DATA

(d) Helical-vane-insert pitch to tube diameter ratio, 6.36

(d-1) Pressure-loss and heat-transfer data.

Air mass flow rate, m, kg/sec	Air inlet bulk temperature, T_1, K	Air average bulk temperature, $\overline{T}$, K	Static-pressure at inlet tap, P^*, N/m^2	Overall static pressure loss, ΔP_z, N/m^2	Maximum helical velocity at outlet tap, $V_{h,w}$, m/sec	Frictional pressure loss, $\Delta P_{f,h}$, N/m^2	Friction factor, f_h, dimensionless	Reynolds number for friction, Re_h, dimensionless	Air bulk temperature at center station, T_{cs}, K	Net heat flux, Q, w/m^2	Inner wall average temperature at center station, $\overline{T}_{w,cs}$, K	Heat-transfer coefficient at center station, h_{cs}, $w/(m^2)(K)$	Reynolds number at center station, $Re_{h,cs}$, dimensionless	Stanton-Prandtl number at center station, $J_{h,cs}$, dimensionless
8.78×10^{-2}	292.4	305.5	2.517×10^{5}	3.088×10^{4}	1.19×10^{2}	2.476×10^{4}	1.84×10^{-2}	2.18×10^{5}	305.6	3.49×10^{4}	352.3	8.19×10^{2}	2.18×10^{5}	2.28×10^{-3}
7.94	298.5	312.2	2.311	2.868	1.20	2.303	1.88	1.94	312.2	3.28	360.4	7.44	1.94	2.29
7.21	298.8	313.0	2.116	2.648	1.20	2.129	1.93	1.76	313.1	3.09	362.8	6.75	1.75	2.29
6.10	299.6	315.6	1.831	2.276	1.18	1.823	1.98	1.48	315.7	2.94	368.9	5.96	1.48	2.39
4.76	300.1	317.6	1.536	1.718	1.10	1.396	2.09	1.15	317.7	2.47	373.3	4.74	1.15	2.43
3.86	300.8	321.2	1.370	1.325	1.00	1.087	2.20	9.24	321.2	2.29	380.3	4.07	9.23×10^{4}	2.57
2.83	298.7	319.4	1.205	8.148×10^{3}	8.05×10^{1}	6.902×10^{3}	2.34	6.79	319.5	1.69	376.6	3.05	6.79	2.63
2.01	300.8	322.0	1.109	4.634	6.09	4.044	2.51	4.79	322.1	1.21	375.0	2.34	4.79	2.84
5.04	301.8	317.3	1.568	1.816×10^{4}	1.14×10^{2}	1.475×10^{4}	2.01	1.22×10^{5}	317.4	2.33	370.7	4.70	1.22×10^{5}	2.28
4.59	292.3	309.0	1.478	1.585	1.06	1.294	2.06	1.13	309.1	2.26	364.1	4.36	1.13	2.33
4.10	294.1	312.6	1.393	1.359	1.01	1.112	2.08	9.99×10^{4}	312.6	2.22	369.3	4.13	9.99×10^{4}	2.47
3.48	295.4	315.1	1.299	1.093	9.21×10^{1}	9.079×10^{3}	2.20	8.44	315.2	1.99	373.8	3.54	8.44	2.49
2.73	292.0	313.1	1.193	7.461×10^{3}	7.67	6.320	2.32	6.65	313.1	1.66	372.7	2.86	6.65	2.56
2.19	295.2	318.9	1.138	5.326	6.51	4.558	2.45	5.28	318.9	1.48	380.4	2.46	5.27	2.73
1.53	296.5	320.7	1.079	2.926	4.73	2.569	2.69	3.67	320.8	1.05	376.7	1.90	3.67	3.03
1.09	296.6	322.4	1.048	1.643	3.44	1.461	2.97	2.59	322.5	7.91×10^{3}	377.9	1.44	2.59	3.23
2.29	299.6	316.5	1.141	5.374	6.61	4.718	2.35	5.54	316.5	1.11×10^{4}	362.4	2.49	5.54	2.65
2.04	300.1	318.8	1.117	4.475	6.03	3.931	2.41	4.90	318.9	1.08	367.8	2.27	4.90	2.72
1.81	300.9	321.8	1.095	3.749	5.53	3.288	2.48	4.33	321.9	1.08	375.4	2.06	4.33	2.77
1.56	297.6	320.5	1.076	2.907	4.80	2.554	2.60	3.73	320.6	1.01	376.2	1.84	3.73	2.89
1.21	299.6	324.7	1.054	1.945	3.86	1.720	2.78	2.88	324.7	8.63×10^{3}	380.7	1.55	2.88	3.12
9.70×10^{-3}	300.2	325.7	1.040	1.336	3.12	1.194	2.99	2.30	325.7	6.99	379.5	1.31	2.30	3.28

(d-2) Adiabatic pressure-loss data.

Air mass flow rate, m, kg/sec	Air inlet bulk temperature, T_1, K	Air average bulk temperature, $\overline{T}$, K	Static-pressure at inlet tap, P^*, N/m^2	Overall static pressure loss, ΔP_z, N/m^2	Maximum helical velocity at outlet tap, $V_{h,w}$, m/sec	Frictional pressure loss, $\Delta P_{f,h}$, N/m^2	Friction factor, f_h, dimensionless	Reynolds number for friction, Re_h, dimensionless
8.39×10^{-2}	295.8	295.2	2.314×10^{5}	2.783×10^{4}	1.14×10^{2}	2.448×10^{4}	1.90×10^{-2}	2.15×10^{5}
7.58	297.0	296.3	2.103	2.553	1.14	2.248	1.94	1.93
6.67	297.2	296.6	1.878	2.266	1.12	2.003	1.99	1.70
6.06	298.2	297.6	1.736	2.049	1.04	1.816	2.02	1.54
5.48	299.0	298.5	1.624	1.839	1.06	1.646	2.09	1.39
4.78	299.2	298.7	1.484	1.544	1.01	1.397	2.14	1.21
3.93	299.7	299.4	1.334	1.169	9.07×10^{1}	1.077	2.21	9.93×10^{4}
3.04	298.1	298.0	1.212	7.939×10^{3}	7.52	7.496×10^{3}	2.37	7.72
1.80	298.0	298.0	1.081	3.280	4.81	3.202	2.61	4.58
4.84	296.0	295.5	1.463	1.517×10^{4}	1.02×10^{2}	1.367×10^{4}	2.03	1.24×10^{5}
4.36	296.9	296.5	1.384	1.310	9.68×10^{1}	1.192	2.07	1.11
3.77	296.9	296.7	1.293	1.070	8.86	9.863×10^{3}	2.15	9.61×10^{4}
3.44	298.1	297.9	1.249	9.207×10^{3}	8.30	8.586	2.18	8.72
3.10	298.0	297.8	1.206	7.865	7.69	7.405	2.24	7.87
2.68	298.7	298.6	1.159	6.212	6.86	5.920	2.31	6.79
2.21	299.6	299.6	1.113	4.510	5.81	4.355	2.42	5.57
1.97	300.1	300.1	1.094	3.727	5.26	3.622	2.48	4.98
1.70	299.8	299.8	1.072	2.883	4.57	2.820	2.57	4.28
1.23	299.7	299.7	1.042	1.665	3.38	1.645	2.78	3.11
2.20	291.4	291.4	1.106	4.262	5.65	4.119	2.36	5.68
1.96	292.5	292.5	1.089	3.516	5.10	3.420	2.43	5.05
1.70	292.9	292.9	1.072	2.771	4.49	2.712	2.51	4.38
1.56	293.3	293.3	1.057	2.386	4.15	2.342	2.56	4.00
1.39	293.3	293.3	1.048	1.976	3.73	1.946	2.64	4.58
1.20	293.6	293.6	1.036	1.528	3.25	1.511	2.72	3.09
9.90×10^{-3}	293.8	293.8	1.028	1.106	2.69	1.097	2.90	2.54
8.84	294.1	294.1	1.024	9.194×10^{2}	2.41	9.137×10^{2}	3.01	2.27
7.69	294.4	294.4	1.020	7.281	2.10	7.246	3.14	1.97
5.38	294.8	294.8	1.013	3.976	1.48	3.967	3.49	1.38
5.50	296.2	296.2	1.013	4.100	1.52	4.090	3.43	1.40
4.91	296.5	296.5	1.013	3.355	1.35	3.348	3.52	1.25
4.24	296.9	296.9	1.011	2.733	1.17	2.729	3.83	1.08

TABLE IV. - PHYSICAL DIMENSIONS OF INSERTS SIMILAR TO THE HELICAL VANE

Type of insert	Insert pitch to tube diameter, Y/D_W	Pitch		Centerbody diameter		Vane thickness or wire diameter	
		Average, cm	Standard deviation, percent	Average, cm	Standard deviation, percent	Average, cm	Standard deviation, percent
Helical vane without centerbody	1.75	3.83	2.0	0	----	0.066	0.19
Wire-wrapped plug	2.915	6.44	2.65	1.33	1.50	.451	.09
Wire-wrapped plug	2.720	6.01	24.5	1.91	.09	.163	.04

NASA-Langley, 1970 —— 1 E-5743

"The aeronautical and space activities of the United States shall be conducted so as to contribute . . . to the expansion of human knowledge of phenomena in the atmosphere and space. The Administration shall provide for the widest practicable and appropriate dissemination of information concerning its activities and the results thereof."

—NATIONAL AERONAUTICS AND SPACE ACT OF 1958

NASA SCIENTIFIC AND TECHNICAL PUBLICATIONS

TECHNICAL REPORTS: Scientific and technical information considered important, complete, and a lasting contribution to existing knowledge.

TECHNICAL NOTES: Information less broad in scope but nevertheless of importance as a contribution to existing knowledge.

TECHNICAL MEMORANDUMS: Information receiving limited distribution because of preliminary data, security classification, or other reasons.

CONTRACTOR REPORTS: Scientific and technical information generated under a NASA contract or grant and considered an important contribution to existing knowledge.

TECHNICAL TRANSLATIONS: Information published in a foreign language considered to merit NASA distribution in English.

SPECIAL PUBLICATIONS: Information derived from or of value to NASA activities. Publications include conference proceedings, monographs, data compilations, handbooks, sourcebooks, and special bibliographies.

TECHNOLOGY UTILIZATION PUBLICATIONS: Information on technology used by NASA that may be of particular interest in commercial and other non-aerospace applications. Publications include Tech Briefs, Technology Utilization Reports and Notes, and Technology Surveys.

Details on the availability of these publications may be obtained from:

SCIENTIFIC AND TECHNICAL INFORMATION DIVISION

NATIONAL AERONAUTICS AND SPACE ADMINISTRATION

Washington, D.C. 20546